Dynamic mitochondrial transcription and translation in B cells control germinal centre entry and lymphomagenesis

Yavuz F Yazicioglu[1]
Eros M Marin[1]
Silvia Galiani[2]
Ewoud B Compeer[1]
Ciaran Sandhu[1]
Moustafa Attar[1]
Michael L Dustin[1]
Alexander J Clarke[1]*

1. Kennedy Institute of Rheumatology, University of Oxford, Oxford, UK
2. MRC Human Immunology Unit, Weatherall Institute of Molecular Medicine, University of Oxford, Oxford, UK

*Lead author

Abstract

Germinal centre (GC) B cells undergo proliferation at very high rates in a hypoxic microenvironment, but the cellular processes driving this are incompletely understood. Here we show that the mitochondria of GC B cells are highly dynamic, with significantly upregulated transcription and translation rates associated with the activity of transcription factor mitochondrial A (Tfam). Tfam, whilst also necessary for normal B cell development, is required for entry of activated GC-precursor B cells into the germinal centre reaction, and deletion of Tfam significantly impairs GC formation, function, and output. Loss of Tfam in B cells compromises the actin cytoskeleton and impairs cellular motility of GC B cells in response to chemokine signalling, leading to their spatial disorganisation. We show that B cell lymphoma substantially increases mitochondrial translation, and deletion of Tfam in B cells is protective against the development of lymphoma in a c-Myc transgenic model. Finally, we show that pharmacologic inhibition of mitochondrial transcription inhibits growth of GC-derived human lymphoma cells, and induces similar defects in the actin cytoskeleton.

Introduction

The germinal centre (GC) reaction is a highly spatially organised process in secondary lymphoid tissue essential for humoral immunity[1]. B cells responding to antigen captured by follicular dendritic cells introduce random mutations in their immunoglobulin genes in a process known as somatic hypermutation (SHM), which occurs in the anatomically defined dark zone (DZ), and are then selected through competitive interaction with follicular T-helper cells (T_{FH}) in the light zone (LZ). GC B cells cycle between these zones, leading to antibody affinity maturation and eventually formation of memory B or plasma cells. During SHM, double-stranded DNA breaks are introduced in immunoglobulin gene loci through the action of activation-induced cytosine deaminase (AICDA). This can give rise to oncogenic mutations, for example the translocation of MYC with *IGH* or *IGL* loci[2]. GC B cells are the origin of most diffuse large B cell lymphomas (DLBCL), the most common non-Hodgkin lymphoma.

The metabolic processes that support GC B cell homeostasis remain incompletely understood. GC B cells are highly proliferative, with division times as short as 4-6 hours, and reside within a hypoxic microenvironment[3–5]. Typically, rapidly proliferating immune cells

mainly use aerobic glycolysis, but GC B cells rely on fatty acid oxidation and oxidative phosphorylation (OxPhos), although to what extent remains somewhat controversial[4–9]. This metabolic phenotype is carried over into a substantial proportion of diffuse large B cell lymphoma (DLBCL), which are also OxPhos dependent[10]. Mitochondria have been demonstrated in vitro to be regulators of B cell signalling through redox-related mechanisms, although whether these studies can be generalised to the hypoxic microenvironment of the GC found in vivo is uncertain[11–13].

Despite evidence of a central role for mitochondria, their dynamics, function, and regulation in GC B cell biology remains largely unknown.

We show that GC B cell mitochondria are highly dynamic organelles, undergoing profound structural changes as they transition through the germinal centre reaction. We find that the mitochondrial translation and transcription factor, *transcription factor A mitochondrial* (TFAM) is dynamically regulated in B cells, and is required for transcriptional and spatial entry into the GC reaction by modulating cellular motility. We also demonstrate using genetically modified mouse models that TFAM is essential for the development of lymphoma, and that pharmacologic inhibition of mitochondrial transcription in human lymphoma cells represents a potential treatment target for human disease.

Results

1. GC B cells undergo extensive mitochondrial remodelling and biogenesis associated with mitochondrial protein transcription and translation

In order to determine mitochondrial density and structure in GC B cells, we first immunised mitochondrial reporter mice expressing GFP and mCherry tagged with a mitochondrial fission-1 (FIS1) targeting sequence (MitoQC)[14], with the T-dependent antigen sheep red blood cells (SRBC), and examined splenic tissue by confocal microscopy and flow cytometry at D12. GFP signal was strongly localised to GL-7$^+$ GCs, and significantly higher than the surrounding B cell follicle (figure 1A-B), which we confirmed by flow cytometry (figure 1C). GC B cells cycle between anatomically defined regions known as the light zone (LZ), in which T cell interaction occurs, and the dark zone (DZ), the site of rapid proliferation and somatic hypermutation. The recently identified grey zone (GZ) represents an intermediate state associated with the G2-M cell cycle phase and expression of metabolism and DNA replication-related genes[15]. Using flow cytometry, we found that the mitochondrial GFP signal was highest in the GZ, followed by the LZ and then the DZ (figure 1C). To examine GC B cell mitochondrial morphology in these regions, we sorted naïve B cells from unimmunised, and LZ, DZ, and GZ GC B cell subsets respectively from MitoQC mice immunised with SRBC (D12) (for gating strategy see S1A), and performed 3D Airyscan confocal imaging. We found highly distinct mitochondrial morphology between naive and GC B cells, with small, fragmented mitochondria in naïve B cells, and large fused mitochondria in GC B cells, most prominently in those from the GZ (figure 1D). Mitochondrial mass assessed by 3D volume analysis was also highest in GZ B cells, followed by LZ and then DZ cells, corresponding with flow cytometry measurements. The MitoQC reporter mouse also allows detection of autophagy of mitochondria (mitophagy), as mCherry is resistant to quenching in the acid environment of the autolysosome. Using multispectral imaging flow cytometry, we screened GC B cells for the presence of GFP$^-$mCherry$^+$ punctae. Although autophagy has been reported in GC B cells[16], we did not identify evidence of active mitophagy (figure S1B). Thirteen protein members of the electron transport chain (ETC) are encoded by mitochondrial DNA and synthesised by the mitochondrial translation machinery[17]. We hypothesised that in order for B cells entering the GC reaction to acquire the high

mitochondrial mass we observed, activation of mitochondrial transcription and translation would be required. Using Aicda-cre × Rosa26-stop-tdTomato reporter mice to label GC B cells, we found markedly increased levels of cytochrome c oxidase subunit 1 (COX1), an enzyme encoded by the *mitochondrially encoded cytochrome c oxidase 1* (*mt-CO1*) gene, and part of ETC complex IV, in the GC (figure 1E). This was confirmed by intracellular flow cytometry, which revealed a substantial increase in COX1 levels in GC B cells, compared to $IgD^{+}GL\text{-}7^{-}$ naïve B cells (figure 1F).

To examine mitochondrial transcription, we next injected mice with 5-ethynyl uridine (5-EU), which is incorporated into actively synthesised RNA, and examined co-localisation with COX1. We detected co-localisation between 5-EU and COX1, which was more prominent in GC B cells, and most often seen in areas of high COX1 expression (figure 1G).

To understand the regulation of this high rate of mitochondrial protein transcription and translation, we examined the expression and distribution of transcription factor A mitochondrial (TFAM) (figure 1G). TFAM is a DNA-binding high mobility box group (HMBG) protein which aids in the packing of the mitochondrial genome into nucleoids, analogous to the role of histone proteins, and also controls transcription and translation of mitochondrial DNA, serving as a regulator of mitochondrial biogenesis[18,19]. Using Airyscan immunocytochemistry in sorted GC B cells, we found TFAM protein organised into punctate structures representing mitochondrial nucleoids, which co-localised with 5-EU (figure 1G). These were more numerous and larger in GC B cells (figure 1H), and had a more elliptical morphology, which is associated with transcriptional activity (figure S1C)[20]. We confirmed the increase in nucleoid number using stimulated emission depletion (STED) super-resolution microscopy (figure 1I).

2. *Tfam* is essential for B cell development and differentiation

TFAM has been shown to have a role in the prevention of long term inflammatory immunosenescence in T cells, but to be dispensable for their development[21,22]. Whether TFAM is important for B cell development or function is unknown. To address this question, we first conditionally deleted *Tfam* in B cells using *Cd79a*-cre (hereafter B-Tfam), which is active from the early pro-B cell stage[23]. Tfam was efficiently deleted (figure S2A). B-Tfam mice appeared healthy, with no clinical signs of immunosenescence or overt autoimmunity. However, B-Tfam mice had a profound reduction in the peripheral B cell compartment, comparatively more marked for follicular than marginal zone B cells (figure 2A). Analysis of B cell development in the bone marrow indicated a failure of progression from the pro- to the pre-B cell stage, which represents an important physiological checkpoint in B cell ontogeny, and few cells were able to express surface immunoglobulin (figure 2B-C)[24]. We noted that heterozygous B-Tfam mice had normal B cell development and an intact peripheral B cell compartment (figure S2B and S2C). We next examined the ability of B-Tfam mice to generate GCs. We immunised B-Tfam mice with SRBCs and analysed GC formation by immunofluorescence and flow cytometry at D12. Anatomical and immunofluorescence examination of B-Tfam spleens revealed smaller and fewer B cell follicles and an almost complete absence of $GL\text{-}7^{+}$ GCs compared to B-WT mice (figure 2D-E), which was confirmed by flow cytometry (figure 2F). Despite the lack of developmental phenotype, *Tfam* heterozygosity in B cells led to a significantly reduced GC response following SRBC immunisation (figure 2G).

3. **GC B cells require TFAM**

Having established a role for TFAM in B cell development, we next focused on its function in the GC reaction. To specifically delete *Tfam* in GC B cells, we generated Aicda-cre × *Tfam* flox × Rosa26-stop-tdTomato × *Prdm1*-mVenus mice (hereafter Aicda-Tfam), which allow simultaneous identification of cells which have expressed *Aicda* (activated, GC, memory B, and plasma cells) and/or currently express Blimp-1 (by detection of the fluorescent reporter proteins tdTomato and mVenus respectively) (figure 3A). Aicda-Tfam mice were immunised with SRBCs and analysed at D12. Immunofluorescent staining of Aicda-Tfam spleen sections demonstrated small GCs in reduced numbers while B cell follicles, immunostained with anti-CD21/35, remained unaltered (figure 3B). Clusters of plasma cells (PCs) in the splenic cords were much smaller in Aicda-Tfam mice, and Blimp1-mVenus^{+}tdTomato^{+} cells were poorly represented, suggesting impairment of GC output (figure 3C). The proportion of CD138^{+} tdTomato^{+} long-lived plasma cells in bone marrow was also significantly lower (figure S3A). We found that the generation of CD19^{+}IgD^{lo}CD38^{-}GL-7^{+} (and correspondingly CD19^{+}IgD^{lo}CD38^{-}tdTomato^{+}) GC B cells was substantially reduced in Aicda-Tfam mice as measured by flow cytometry (figure 3D-E). We also confirmed a reduction in Blimp1-mVenus^{+}tdTomato^{+} post-GC plasma cells (figure 3F).

Next, we examined antigen-specific GC formation by immunising mice with 4-hydroxy-3-nitrophenylacetyl-chicken gamma globulin (NP-CGG). After 14 days, the proportion and absolute numbers of NP-binding GC B cells were much reduced in Aicda-Tfam mice (figure 3G and S3B). Affinity maturation was also compromised, with decreased binding of antibodies to $NP_{1\text{-}9}$ compared with $NP_{>20}$ (figure 3H and S3C). To determine whether the defect we saw in Aicda-Tfam mice was B cell-intrinsic, we generated mixed competitive bone marrow chimeras with CD45.1 congenic wild type mice. Aicda-Tfam GC B cells were outcompeted by CD45.1 wild type cells, compared with Aicda-WT controls in spleens and Peyer's patches (figure S3D).

Mitochondria play a central role in the regulation of apoptosis, but surprisingly the apoptosis rate detected by means of activated caspase 3 staining in Aicda-Tfam GC B cells was comparable with that of Aicda-WT controls (figure 3I). In situ terminal deoxynucleotidyl transferase dUTP nick end labelling (TUNEL) also demonstrated unaltered apoptotic cell frequency (figure 3J). We next evaluated the cell cycle dynamics of Aicda-Tfam GC B cells, first assessing G2 and M stages by measuring cyclin B1 and phospho-H3 (p-H3) expression, which were not significantly different between Aicda-Tfam and Aicda-WT mice (figure 3K). 5-ethynl-2-deoxyurine (EdU) incorporation into DNA, which detects S phase, was also unaffected (figure 3L).

We also confirmed that *Tfam* deletion did not affect proliferation or cell viability in vitro, by treating B cells from *Tfam* flox × Rosa26-stop-tdTomato or wild type Rosa26-stop-tdTomato mice with TAT-cre recombinase, then stimulating them with anti-IgM, agonistic anti-CD40, and IL-4 for four days. *Tfam* was effectively deleted in tdTomato^{+} cells, but there was no difference in dilution of CellTrace Violet or in viability (figure S3F-G).

Despite a significant reduction in GC B cell formation in Aicda-Tfam mice, we were therefore unable to demonstrate increased apoptosis, or defects in the cell cycle. There was however, a modest reduction in the level of the GC transcriptional regulator BCL6 in GC B cells from Aicda-Tfam mice (figure 3M).

4. **TFAM controls transcriptional entry into the GC program**

In order to examine the effects of *Tfam* deletion on the transcriptional program of GC B cells, we performed combined single cell RNA and V(D)J sequencing. We immunised Aicda-Tfam and Aicda-WT mice with NP-CGG, and sorted CD19^{+}tdTomato^{+} cells at D14 (figure 4A). This population includes any B cell that has expressed *Aicda*, and so will be expected to include pre-GC, GC, memory, and plasma cells. We sequenced a total of 9,948 cells from Aicda-Tfam and 9,667 cells from Aicda-WT mice. Cells were clustered following integration of the two experimental groups, and clusters were identified by canonical markers (figure 4B-C). We identified 9 shared clusters, broadly separated into B cells from GC, CD38^{+} non-GC, and plasma cell populations. Cluster 0 (C0), which expressed markers of immaturity suggestive of an activated precursor (AP) state (*Ighd*, *Ccr6*, *Gpr183*, *Cd38*, *Sell*, and low levels of *Bcl6*), was significantly expanded in Aicda-Tfam compared with Aicda-WT mice (figure 4D).

Examination of differential gene expression in C0 revealed, as expected, broad dysregulation of mitochondrial gene expression in Aicda-Tfam mice, in keeping with the function of *Tfam* as an activator of mitochondrial transcription (figure 4E). Pathway analysis comparing multivariate distributions (SCPA) [25] demonstrated substantial downregulation of translation initiation and elongation gene sets (figure 4F). Gene components of the AP-1 signalling pathway *Jun*, *Junb*, and *Fos* were all significantly upregulated (figure 4G). The AP-1 pathway is broadly upregulated by cellular stress signalling, reactive oxygen species, and in response to environmental cues[26,27].

Analysis of the main GC cluster (C1) demonstrated as before, dysregulation of mitochondrial and ribosomal gene transcription, with upregulation of *Jun, Fos,* and *Junb* (figure 4H-I). Notably increased in Aicda-Tfam cells was *Rgs1* (regulator of G-protein signaling-1), a GTPase activating protein which has an important role in the negative regulation of cell movement in response to chemokines (e.g. CXCL12)[28,29] (figure 4J). Downregulated was *Coro1a* (coronin-1), which encodes an actin-binding protein required for cell migration [30], and *Arpc3* (actin-related protein 2/3 complex subunit 3), which mediates branched actin polymerisation and actin foci formation[31]. We also detected a reduction in *Mef2b*, which regulates GC enhancer genes by transactivating *Bcl6*, and is important for GC B cell positioning.

Across other clusters the dysregulation of mitochondrial and ribosomal genes in Aicda-Tfam cells was repeated, with no evidence for compensatory upregulation of glycolysis or other metabolic pathway genes. Cluster 6 within the GC supercluster was characterised by expression of interferon response genes, and was subjectively expanded in Aicda-Tfam mice, although this did not reach statistical significance. This may represent a response to mitochondrial DNA leaking into the cytoplasm, which has been previously noted in Tfam deficient cells[32].

We next examined B cell clonality by evaluation of V(D)J sequences. Since we sorted all tdTomato^{+} B cells, the overall clonal diversity of all samples remained high (figure 4K). As expected in the anti-NP immune response, V_H1-72 gene usage was dominant (figure 4L). However, there was more diversity in Aicda-Tfam mice, with fewer larger clones, suggesting that there was less ability for evolution of dominant clones. There was significantly less somatic hypermutation in Aicda-Tfam B cells (figure 4M).

5. **TFAM is required for GC B cell commitment**

Given the accumulation in immunised Aicda-Tfam mice of activated precursor B cells with high expression of *Sell* (L-selectin), *Ccr6*, and a GC transcriptional profile suggestive of altered cell trafficking and cytoskeleton dynamics, we hypothesised that *Tfam* is required for activated B cells to enter the GC and remain appropriately spatially positioned.

We first confirmed an expansion of APs, defined by tdTomato and IgD expression, in Aicda-Tfam mice following NP-CGG immunisation (figure 5A). We found that in Aicda-WT mice, a lower proportion of AP B cells bound NP compared to GC B cells, and did so with lower affinity, indicating their pre-GC state (figure S5A). We then examined splenic sections of immunised Aicda-Tfam mice under high magnification (figure 5B). We found highly disorganised GC architecture, with poor GC B cell compartmentalisation, and within the follicle, there were relatively many more tdTomato^{+}IgD^{+} B cells in Aicda-Tfam mice.

There was dynamic expression of TFAM, with a peak at the AP stage, which subsided following GC entry, and a progressive increase in COX1 (figure 5C-D). We next examined B-Tfam mice immunised with SRBC, defining APs as IgD^{+}GL-7^{int} (figure 5E). The AP population was also markedly expanded.

We then measured the metabolic consequences of Tfam deletion on APs and GC B cells, quantifying protein translation rate by the incorporation of the puromycin analogue O-propargyl-puromycin (OPP) as a proxy for metabolic capacity, as recently reported[33] (figure 5F-G). The addition of inhibitors of glycolysis (2-deoxyglucose) or ATP synthetase (oligomycin) which disrupts the electron transport chain allows the relative contributions of these metabolic pathways to be estimated. GC B cells had significantly higher basal OPP incorporation than AP B cells, reflecting their high levels of metabolic activity (figure 5F). Oligomycin treatment led to a substantial reduction in OPP uptake in GCs compared to APs, which was not affected by Tfam deletion. However, mitochondrial dependence was reduced in B-Tfam APs, with an equivalent increase in glycolytic capacity. This effect was seen to a far lesser extent in GC B cells (figure 5G). A similar trend was also observed with glucose dependence and fatty acid/amino acid oxidation (FAO/AAO) capacity of APs and GC B cells (figure S5B).

We next examined the effect of Tfam deletion on mitochondrial translation in APs. We found significantly reduced COX1 expression in B-Tfam APs, with an increase in the nuclear-encoded enzyme succinate dehydrogenase B (SDHB), which forms part of the ETC complex II, suggesting an attempted compensatory mechanism for impaired translation of mtDNA (figure 5H-I).

Overall, our results showed that expression of TFAM was necessary to program APs for GC entry, at least in part by allowing mitochondrial translation, which represents an important checkpoint in humoral immunity.

6. **Tfam deletion disrupts GC spatial organisation and impairs cell mobility**

The germinal centre is a spatially organised structure divided into light and dark zones. We found that Aicda-Tfam GCs were poorly compartmentalised, with smaller DZs on immunohistochemistry (figure 6A), and a disrupted DZ/LZ ratio measured using flow cytometry (figure 6B).

Positioning of B cells in the GC is controlled by the chemokines CXCL12 and CXCL13, which promote migration to the DZ and LZ, respectively[34]. Since our preceding data indicated that AP B cells need TFAM to enter the GC, and given the transcriptional profile of Aicda-Tfam GC B cells was suggestive of cytoskeletal and mobility defects, we hypothesised that TFAM was required for proper cellular positioning in GCs.

We examined the cellular actin network of TFAM-deficient B cells, and found a significant increase in filamentous actin in Aicda-Tfam B cells (figure 6C-D), which was also evident in B-Tfam B cells (figure S6A-B). Rearrangement of the actin cytoskeleton is critical for B cell migration[35], and to understand if Tfam deletion compromised GC B cell motility, we performed a transwell migration assay to determine chemotaxis in response to the chemokines CXCL12 and CXCL13. We found that Aicda-Tfam GC B cells migrated poorly, with significantly reduced chemotaxis compared to Aicda-WT cells (figure 6E).

B-cell receptor (BCR) and chemokine-driven cytoplasmic calcium mobilisation critically regulates F-actin organisation in B cells[36]. As mitochondria are an important reservoir of intracellular calcium[37], we asked whether Tfam deletion lead to dysregulated intracellular calcium levels. Following CXCL12 stimulation, B220$^+$ B cells from B-Tfam mice failed to sustain peak cytoplasmic calcium levels (Figure 6F), which we also observed after BCR stimulation with anti-IgM antibodies (figure 6G & S6C). Interestingly, we also detected a significant upregulation in levels of the mitochondrial calcium uniporter (MCU), suggesting elevated calcium uptake capacity in B-Tfam B cells, whereas CD3$^+$ T cells showed comparable MCU expression (figure 6H & S6D).

Mitochondrial ROS were also substantially increased in B-Tfam naïve and APs (figure 6I & S6E). ROS activate the AP-1 signalling pathway[27], and this observation was therefore consistent with the transcriptional profile of Aicda-Tfam AP B cells.

Our data collectively suggest that TFAM is required for proper cellular motility, and that this effect is independent of impaired ATP production, but associated with ETC dysfunction and increased mitochondrial ROS.

7. *Tfam* deletion in B cells abrogates the development and progression of lymphoma

Having demonstrated an essential role for TFAM in B cell development and entry into the GC, we next asked whether it was required for the development of lymphoma. One of the most common mutations giving rise to DLBCL is translocation of *MYC* to immunoglobulin gene loci, leading to its unregulated expression. c-Myc is a key transcription factor regulating cell cycle and growth, cellular metabolism, and mitochondrial biogenesis[38]. We reasoned that deletion of *Tfam* would counter the oncogenic effects of c-Myc overexpression. We employed the well-established Eμ-Myc transgenic mouse model of lymphoma, in which *Myc* is expressed under the control of the *Igh* enhancer[39]. Eμ-Myc mice develop lymphoma with high penetrance from a median age of 11 weeks. To understand what effects overexpression of Myc had on mitochondrial translation, we transferred established lymphoma cells from Eμ-Myc mice (CD45.2) into wild type CD45.1 congenic hosts, to allow us to compare B cells from the same environment (figure 7A). We found very markedly higher expression of COX1 in CD45.2 lymphoma cells compared with wild type B cells, with significantly upregulated TFAM (figure 7B-C).

We next generated *Cd79a*-cre × *Tfam* flox × Eμ-Myc mice (B-Tfam-Myc), to delete *Tfam* in B cells. B-Tfam-Myc mice were completely protected from the development of lymphoma

during the observation period of 30 weeks, compared with *Tfam* flox × Eμ-Myc controls, which had a median survival of 10 weeks, or *Cd79a*-cre × *Tfam* het × Eμ-Myc heterozygous mice (figure 7D).

Finally, to establish whether inhibition of mitochondrial transcription and translation might be a therapeutic target in human lymphoma, we treated Daudi B cell lymphoma cells (originally arising from Burkitt lymphoma) with IMT1, a specific inhibitor of mitochondrial RNA polymerase (POLRMT), which functions along with TFAM to initiate mitochondrial RNA transcription[40]. We found that treatment with IMT1 led to a progressive reduction of COX1 levels, with increasing COX1:SDHB mismatch (figure 7E-F). Imaging of Daudi cells treated with IMT1 revealed mitochondrial enlargement, and confirmed the loss of COX1 (figure 7G). IMT1 reduced cell proliferation, inhibited cell cycle progression, increased mitochondrial ROS levels, and recapitulated the F-actin defect we observed with *Tfam* deletion, also leading to increased mitochondrial ROS levels (figure 7H-K, S7A). To inhibit mitochondrial translation we used the oxazolidinone antibiotic chloramphenicol[41]. Chloramphenicol reduced COX1 expression, and also increased F-actin in Daudi cells (figure 7L-M). Cell growth was substantially reduced (figure 7N).

These results define high rates of mitochondrial translation enabled by *Tfam* expression as an essential requirement for the development of B cell lymphoma, and show the therapeutic potential of mitochondrial RNA polymerase inhibition in human disease.

Discussion

Here we show that upon entry to the GC, B cells dramatically remodel their mitochondria, increasing their mass and radically altering their morphology. As part of this transition, mitochondrial translation is highly active, and we demonstrate that the nuclear-encoded mitochondrial transcriptional and translational regulator TFAM is not only required for B cell development, but also for their entry into the GC program, proper spatial anchoring, and for the subsequent development of lymphoma.

GC B cells have a highly distinct metabolism, predominantly relying on OxPhos despite their very rapid rate of proliferation in a hypoxic microenvironment[6,8]. In order for rapidly dividing cells to maintain high mitochondrial mass in the face of dilution to their daughters, a high rate of mitochondrial protein translation and division must be maintained. We were surprised to find that TFAM is required for entry into the GC program itself, and when deleted there is an accumulation of B cells with an activated precursor phenotype, which have expressed AID, but maintain markers of immaturity. It has recently been shown that the TCA metabolite α-ketoglutarate is upregulated by IL-4 in B cells, and that this leads to epigenetic alteration of the *Bcl6* locus[9]. It is therefore possible that TFAM is required for an initial burst of mitochondrial biogenesis to facilitate GC program entry.

Interestingly, GC B cells themselves have relatively reduced expression of TFAM compared to AP B cells, despite high levels of mitochondrial mass and dilution. TFAM is responsible for packaging mitochondrial DNA into structures known as nucleoids, and also for maintenance of mtDNA copy number. The relative ratio of TFAM to mtDNA in nucleoids can dictate the expression of mitochondrial genes, based on the degree of genomic compaction[20]. It has been demonstrated that following activation in vitro, B cells have reduced mtDNA copy number and the number of nucleoids per mitochondrion drops, but their area increases[42]. In our transcriptional data, APs, in which *Tfam* deletion is likely to be recent, display generalised disruption of mitochondrial gene expression, with both up and downregulation.

In GC B cells however, mitochondrial transcription is generally reduced in the absence of *Tfam*.

Surprisingly, despite a significant effect on GC B cell differentiation, deletion of TFAM had only a small effect on the metabolic state of GC B cells, whilst clearly affecting AP B cells. AP B cells increased their glycolytic capacity substantially, and dramatically upregulated expression of SDHB, which did not occur to a significant degree in GC B cells. One potential explanation is that BCL6 has been found to repress expression of glycolysis genes[43], and may therefore attenuate compensatory mechanisms.

Tfam deletion led to significant defects in calcium signalling, with upregulation of the MCU suggesting mitochondrial calcium sequestration. This was associated with defective B cell chemotaxis, and failure of spatial confinement associated with impaired migratory capacity to CXCL12 and 13. Consistent across genetic or pharmacologic interference with mitochondrial transcription and translation was an increase in F-actin. Dynamic actin cytoskeletal modification is essential for normal cell movement, and its probable disruption through defective calcium signalling seen following TFAM deletion is likely to account for the positioning and motility defects we observed. This adds weight to the idea that mitochondria are intimately linked to cytoskeletal function, and that this role may operate independent of ATP generation[44]. There was also an accumulation of ROS in Aicda-Tfam APs, and this may also lead to abnormal cell movement, and may also contribute to the F-actin abnormalities seen[45].

Although we have directly established the importance of TFAM as a regulator of B cell development and activation, the factors driving the counterintuitive switch to OxPhos in GC B cells remain to be uncovered, as do the signalling mechanisms controlling the differences in mitochondria we observed between GC microenvironments. Disruption of mitochondrial integrity also induces a phenotype associated with immune aging, and to what extent the mechanisms we describe might hold true in the diminished humoral immune response seen with age is another area deserving of further exploration[22].

We show that deletion of *Tfam* is sufficient to completely prevent the development of Myc-driven lymphoma. Although loss of Tfam at an early developmental stage leads to B cell lymphopenia, and therefore the pool of B cells which may become malignant is reduced, the high penetrance of the model contrasted with the complete protection against lymphoma suggests this is insufficient to explain the phenotype we observe. How TFAM acts to support lymphomagenesis requires further study, but may be associated with its promotion of mitochondrial translation[46]. Our observation that inhibition of mitochondrial transcription and translation reduces growth of lymphoma cells suggest that this should be prioritised as a therapeutic target.

Materials and methods

Mice

B6.Cg-*Tfam*$^{tm1.1Ncdl}$/J (JAX:026123), B6.C(Cg)-*Cd79a*$^{tm1(cre)Reth}$/EhobJ (JAX: 020505), B6.129P2-*Aicda*$^{tm1(cre)Mnz}$/J (JAX:007770), B6;129S6-*Gt(ROSA)26Sor*$^{tm9(CAG-tdTomato)Hze}$/J (Ai9, JAX:007905), and B6.Cg-Tg(IghMyc)22Bri/J [Eμ-Myc] **(**JAX 002728) were purchased from Jackson Laboratories. Tg(Prdm1-Venus)1^{Sait} [Blimp1-mVenus] (MGI:3805969) was a kind gift from Mitinori Saitou (Kyoto University). Gt(ROSA)26Sor$^{tm1(CAG-mCherry/GFP)Ganl}$ (MitoQC) was a kind gift from Ian Ganley (University of Dundee). B6.SJL.CD45.1 mice were provided by central breeding facility of the University of Oxford. Male and female mice between the ages of 6-15 weeks were used. Mice were bred and maintained under specific pathogen-free conditions at the Kennedy Institute of Rheumatology, University of Oxford. All procedures and experiments were performed in accordance with the UK Scientific Procedures Act (1986) under a project license authorized by the UK Home Office (PPL number: PP1971784).

Immunisation

For SRBC immunisation, 1 ml of sterile SRBCs (ThermoFisher) were washed twice with 15ml of ice-cold PBS and reconstituted in 3ml of PBS. In some experiments, an enhanced SRBC immunisation method was followed to maximise GC B cell yield by immunising mice with 0.1 ml SRBC on day 0 followed by 0.2 ml second injection on day 5 [47]. For protein antigen immunisations, 50μg $NP_{(30-39)}$-CGG (Biosearch Tech) was mixed with Alum (ThermoFisher) at a 1:1 ratio and rotated at room temperature for 30 mins before intraperitoneal injection. For NP-CGG and SRBC-based immunisations, day 14 and day 12 were used as read-out time points, respectively unless specified otherwise.

Cell sorting

Naïve B cells were isolated using Pan B cell Isolation II Kit (Miltenyi) or anti-CD43 Microbeads (Miltenyi) according to the manufacturer's protocol. Purity was >90% validated by flow cytometry. Isolation of DZ-LZ-GZ subsets of GC B cells was performed via fluorescence activated cell sorting (FACS).
For some experiments, we isolated untouched GC B cells through a MACS-based isolation protocol as described in by Cato et al. [48]. Briefly, spleens were harvested from SRBC-immunised mice, and single cell suspensions were prepared in ice cold MACS isolation buffer (PBS with 0.5% BSA + 2mM EDTA) followed by ACK RBC lysis (Gibco) for 4 mins at RT. After washing, cells were labelled with anti-CD43 microbeads (Miltenyi) and biotinylated antibodies against CD38 (eBioscience) and CD11c (eBioscience), followed by incubation with anti-Biotin microbeads, and subsequently run through a MACS LS column. Purity was validated via flow cytometry and immunocytochemistry (ICC) and exceeded 95%.
For scRNAseq experiment, spleens were crushed using rough ends of microscope slides to maximise cell yield. Subsequently, non-B cells were depleted using pan B cell Kit II (Miltenyi). Enriched cells were then labelled with viability dye, FcBlock and surface flow antibodies including markers for Dump channel exclusion (anti-CD3, anti-Gr1 and anti-CD11c) and sorted by BD Aria FACS.

Flow Cytometry and ImageStream

Flow cytometry was performed as previously described (Yazicioglu et al., 2018). Briefly, spleens were injected with ice cold PBS and mashed through a 70 μm strainer or crushed between the frosted ends of microscope slides. RBCs were depleted by incubating splenocytes with ACK Lysis Buffer (Gibco) for 3-4 mins at RT. Single cell suspensions in PBS were labelled with Fixable Viability Dye eFluor™ 780 (eBioscience) followed by FcBlock (5 mins) and surface antibodies in FACS buffer (PBS + 0.5% BSA and 2 mM EDTA) (30 mins on ice). For intracellular staining, we performed cell fixation at RT with 4% freshly prepared PFA for 15 mins and used methanol-based permeabilization (90% ice cold for 10 mins on ice with frequent vortexing) unless specified otherwise. Phalloidin-based F-Actin staining was performed using BD Perm/Wash reagent (Cat. No. 554723) following 4% PFA fixation. For in vivo cell cycle analysis, 5-ethynyl-2'-deoxyuridine (EdU) (1mg) was injected intraperitoneally and mice were sacrificed after 2.5 h. Cells were then labelled using Click chemistry following manufacturer's instructions (Click iT Plus EdU Flow cytometry kit, Thermo Fisher). FxCycle Violet (Thermofisher) reagent was used for cell cycle characterisation. For Mitotracker Deep Red (MTDR)(Thermofisher) and mitochondrial superoxide deep red (mtSOX)(Dojindo) uptake, following viability dye and surface staining, cells were resuspended in warm complete RPMI supplemented with MTDR (100nM) or mtSOX (10µM) and incubated for 30 mins at 37°C. Cell were washed twice before flow cytometry acquisition. Flow cytometry was performed on BD Fortessa X-20 and/or LSR II instruments (BD). For imaging cytometry, single cell suspensions were prepared from Mito-QC PPs, stained with live-dead dye, and surface markers followed by 4% PFA fixation. Washed cells were then resuspended in 50µl FACS Buffer and run on Amnis ImageStream X Mark II Imaging Flow Cytometer and analysed with IDEAS (EMD Millipore) and FCS Express software (v7.12).

Flow cytometry

Antibody/reagent & fluorochrome	**Clone**	**Dilution**	**Manufacturer**
Anti-CXCR4 APC	REA107	1:40	Miltenyi Biotec
Anti-CD19 BV510	6D5	1:200	Biolegend
Anti-B220 BV510	RA3-6B2	1:200	Biolegend
Anti-CD38 PECy7	90		
Anti-CD138 BV421	281-2	1:100	Biolegend
Anti-CD138 AF647	281-2	1:100	Biolegend
Anti-CD86 BV421	GL-1	1:100	Biolegend
Anti-CD86 BV785	GL-1	1:75	Miltenyi Biotec
Anti-CXCR4 eFluor 450	2B11	1:50	Thermofisher
Anti-IgD BV510	11-26c.2a	1:200	Biolegend
Anti-IgD BV650	11-26c.2a	1:400	Biolegend
Anti-IgD AF700	11-26c.2a	1:400	Biolegend
Anti-IgM PECy7	RMM-1	1:200	Biolegend
Anti-CD21/35 PE	7E9	1:75	Biolegend
Anti-BP-1 APC	6C3	1:40	Miltenyi Biotec
Anti-CD23 BV421	B3B4	1:200	Biolegend

Anti-CD43 PE	S11	1:200	Biolegend
Anti-CD24 PacBlue	M1/69	1:200	Biolegend
Anti-GL7 AF647	GL7	1:75	Biolegend
Anti-GL7 AF488	GL7	1:75	Biolegend
Anti-GL7 PacBlue	GL7	1:75	Biolegend
Anti-Gr1 APC Cy7	RB6-8C5	1:100	Biolegend
Anti-CD3 APC Cy7	17A2	1:100	Biolegend
Anti-cyclin B1	V152	1:20	Biolegend
Anti-cleaved caspase 3 (Asp175) unconjugated	9661	1:750	Cell signalling
Anti-phospho histone 3 AF488	D2C8	1:800	Cell signalling
Anti-SDHB AF647	21A11AE7	1:100	Abcam
Anti-COX1 AF488	1D6E1A8	1:100	Abcam
Anti-TOMM20 unconjugated	EPR15581-54	1:100	Abcam
Anti-TFAM unconjugated	EPR23548-120	1:600	Abcam
Goat Anti-Rabbit IgG (H&L) SuperClonal antibody AF488	Cat: A27034	1:500	ThermoFisher
Goat Anti-Rabbit IgG (H&L) SuperClonal antibody AF647	Cat: A55055	1:500	ThermoFisher
PE Donkey anti-rabbit IgG (minimal x-reactivity) Antibody	Cat: 406421	1:200	Biolegend
Fixable viability dye eFluor780		1:1000	Thermofisher
Fixable viability dye Aqua		1:1000	Thermofisher
Anti-CD16/32 (Fc Block)	2.4G2	1:200	BD

NP conjugation

Briefly, 1mg of natural allophycocyanin protein (APC) (Stratech Scientific Ltd) was transferred into Slide-A-Lyzer™ MINI Dialysis Device, 3.5K MWCO (Thermofisher, Cat: 69550) and dialysed for 5 hours, overnight, then for 4 hours in 1L 3% $NaHCO_3$ at 4°C. NP-Osu (Biosearch) was dissolved in dimethylformamide (DMF) to a concentration of 10mg/ml while vortexing. The NP-Osu was added to the dialysed APC at a ratio of 20µg:1 mg (NP-Low conjugation) and 80µg:1 mg (NP-High conjugation) and rotated at RT for 2 hours, protected from light. The NP-APC conjugates were then dialysed in 1L 3% NaHCO3 at 4°C overnight before dialysis in 1L PBS overnight. NP probes were stored at 4°C in the dark until use.

IHC

Harvested spleens were immediately transferred to Antigenfix (DiaPath) solution and fixed overnight at 4°C. The next day, spleens were washed in PBS followed by overnight incubation in 30% sucrose (in PBS) at 4°C for cryoprotection. On the following day, spleens were snap frozen in 100% methanol on dry ice and stored at -80°C until cryosectioning.

Cryosectioned (8-12µm) slides were then rehydrated in PBS at RT, permeabilised, and blocked in PBS containing 0.1% Tween-20, 10% goat serum, and 10% rat serum at RT for two hours. For panels requiring intracellular detection, Tween-20 was replaced by 0.5% Triton X-100. All primary antibody staining was performed overnight at 4°C in PBS supplemented with 2% goat serum and 0.1% Triton X-100, and secondary staining was performed at RT for 2 hours next day. TUNEL imaging was performed the Click-iT Plus TUNEL in situ imaging kit (Thermo). Slides were mounted with Fluoromount G (Southern Biotech) and imaged by Zeiss LSM 980. For in vivo measurement of RNA synthesis, 2mg of 5-ethynyl uridine (5-EU, Sigma) was injected intraperitoneally at D12 following SRBC immunisation, and mice were analysed after 1h.

NP-ELISA

Briefly, sera obtained from mice (NP-CGG day 14) were incubated for 1 hour in NP-BSA (NP_2 or $NP_{<20}$)-coated Elisa plates at 1:200 dilution. After serial washes, goat anti-mouse IgG1 (alkaline phosphatase-conjugated) detection antibody was added and incubated for 1 hour. Plates were then developed with AP substrate for 30 mins and read on FLUOstar Omega plate reader.

ICC

0.5-1×10^6 sorted GC B cells and/or naïve B cells were transferred onto 18mm coverslips coated with poly-L-lysine (Merck) and incubated for 10 mins at 37°C to ensure cell attachment. Cells were then fixed in prewarmed 1× PHEM buffer (60mM PIPES, 25mM HEPES, 10mM EGTA, and 4mM MgSO4·7H20) with 4% PFA for 10 mins at 37°C, followed by permeabilization and blocking in 0.2% Triton X-100 with 10% goat serum for 30 mins. Primary antibody labelling was performed overnight at 4°C, and secondary antibody staining for 45 mins at RT.
For the mitochondrial transcription assay based on 5-ethynyl uridine (EU) incorporation, isolated untouched naïve B cells and GC B cells were resuspended in complete RPMI supplemented with 1mM EU and transferred to 18mm coverslips coated with poly-L-lysine. Following a 45 mins incubation, cells were briefly washed and fixed in warm 4% PFA diluted in PHEM Buffer. Following permeabilization and blocking for 30 min, incorporated EU was detected by the Click-iT™ RNA Alexa Fluor™ 594 Imaging Kit (Thermo Fisher). Intracellular antibody labelling was performed after the Click reaction, to minimise the interference of Click reagents with fluorochromes. 4′,6-diamidino-2-phenylindole (DAPI) (Sigma) staining was performed at 1µM at RT for 5 mins, followed by a brief wash and mounting in Fluoromount G (Southern Biotech). When GC B cells were isolated from Aicda-WT and Aicda-Tfam mice, tdTomato reporter signal was used to filter out contaminating non-GC B cells to refine image analyses.

IHC & ICC

Antibody & fluorochrome	Clone	Dilution	Manufacturer
Anti-CD38 AF647	90	1:50	Biolegend
Anti-CD21/35 AF647	7E9	1:75	Biolegend
Anti-IgD AF647	11-26c.2a	1:50	Biolegend

Anti-GL7 AF647	GL7	1:50	Biolegend
Anti-GL7 AF488	GL7	1:50	Biolegend
Anti-GL7 PacBlue	GL7	1:50	Biolegend
Anti-SDHB AF647	21A11AE7	1:75	Abcam
Anti-COX1 AF488	1D6E1A8	1:100 (IHC) 1:500 (ICC)	Abcam
Goat Anti-Rabbit IgG (H&L) SuperClonal antibody AF488	Cat: A27034	1:500	ThermoFisher
Goat Anti-Rabbit IgG (H&L) SuperClonal antibody AF647	Cat: A55055	1:500	ThermoFisher
Anti-TOMM20 unconjugated	EPR15581-54	1:500	Abcam
Anti-TFAM unconjugated	EPR23548-120	1:600	Abcam

Image analysis

Zen Blue (v3.4, ZEISS) and ImageJ softwares were used for image analyses. For the determination of GC properties in splenic sections, tdTomato and/or GL-7 signals were used as a reference to identify GCs, and IgD for naïve B cell follicles. Defined areas were introduced as Region of Interests (ROIs) using the Analyse Particles function. Mitochondria were segmented based on Mito-GFP or COX1 signal, and subsequently area and signal intensity calculations were performed using the Analyse Particles function in ImageJ. For 3D volumetric analyses of mitochondria, the 3D Objects Counter function was used. Mitochondrial 5-EU incorporation is quantified first by identifying mitochondrial area based on thresholded COX1 signal. Background noise in the 5-EU channel was removed using Subtract Background (Rolling ball radius 20 pixels) function. Areas outside of the mitochondrial ROIs were removed, and the remaining 5-EU integrated signal density was determined by the 3D Objects Counter function. 3D TFAM-mitochondrial nucleoid complexes were enumerated by 3D Suite [50]. Briefly, local maxima of TFAM signals were determined for each z-slice using 3D Fast Filters (kernel x, y and z 1px each) which were then fed into a 3D Spot segmentation module with local thresholded Gaussian fit (Radius max 10 px, SD value 1.50). For DZ/LZ analyses in tissue sections, the nesting function in Zen Blue was used by identifying tdTomato$^+$ GCs as ROIs. The CD21/35 signal was then used to calculate the area of the LZ. Normalised DZ area was quantified as follows: (GC area – LZ area) / GC area. Calculation was performed for each individual GC pooled from splenic sections. GCs with >0.95 values were excluded as not including any representative LZ area. Airyscan reconstruction was performed in Zen Blue software with Medium filter setting. ImageJ Macro codes used for image analyses are available upon request.

STED microscopy

STED imaging was performed using a Leica TCS SP8 laser scanning STED system equipped with oil objective (HC PL APO 100× NA 1.40) and a 775nm depletion laser. Isolated naïve and GC B cells labelled with anti-TFAM Alexa Fluor 647 (AF647) were imaged in confocal and STED mode sequentially. COX1 labelled with AF488 was imaged subsequently in confocal mode to define mitochondrial area. Acquired STED images were deconvoluted using Deconvolution Express mode with Standard setting in Huygens Essential software (v22.04) (Scientific Volume Imaging, Hilversum, Netherlands).

Quantification of metabolism by OPP incorporation

The details of this technique were published previously [33]. Briefly, splenocytes were split into 4 groups and incubated for 30 mins with or without metabolic inhibitors (1µM oligomycin and 1mM 2DG, both from Merck) and their combinations in 96 well plate at 37°C. Alkynylated puromycin analog OPP (20µM) (Thermofisher) was then directly added to the wells for an additional 30 mins incubation. Subsequently, cells were washed and labelled with live/dead viability dye and surface antibodies, after which they were fixed with 4% PFA. Click Chemistry labelling was performed according to Click-iT™ Plus OPP Alexa Fluor™ 647 Protein Synthesis Assay Kit (ThermoFisher).

In vitro mouse primary B cell culture

B cells were isolated from spleens of unimmunised Tfam-floxed and wild type mice carrying the Rosa26-stop-tdTomato allele without Aicda-Cre using the Pan B cell isolation kit II (Miltenyi). TFAM was deleted by TAT-Cre recombinase (1.5µM, Merck) in serum-free complete RPMI (supplemented with 2mM GlutaMAX, 1mM pyruvate, 10mM HEPES, 100 IU/ml Penicillin/Streptomycin and 50µM 2-mercaptoethanol) for 45 mins at 37°C and 5% CO_2. CellTrace violet dye at 10µM (Thermofisher) was added directly after 30 mins of TAT-Cre incubation and incubated for 15 min at 37°C. Cells were washed three times with 10% FBS containing complete RPMI, and live cells were counted manually using Trypan Blue exclusion of dead cells. 10^5 live B cells were cultured in U-bottom 96-well plates with anti-IgM (1µg/ml, Jackson Immuno), anti-CD40 (1µg/ml, Miltenyi) and IL-4 (40ng/ml, Peprotech) stimulation for four days at 37°C in a humidified incubator with 5% CO_2.

Transwell migration assay

5×10^5 enriched total B wells were placed in a 6mm transwell chamber with 5µm pore size (Corning, cat: 3421) and incubated at 37°C for two hours in the presence of murine CXCL12 (200ng/ml, Biolegend) or CXCL13 (1µg/ml, Biolegend) in complete RPMI. Relative migration index was calculated as follows: percentage of GC B cells ($CD38^-$ $GL\text{-}7^+$ $tdTomato^+$) in total input cells divided by the percentage of GC B cells in migrated live total cells.

Cytoplasmic calcium assay

Due to the time and temperature sensitive nature of calcium dyes, experiments were performed in four batches such that one wild type and one B-Tfam mouse spleen were processed in each replicate. Single cell suspensions were prepared from spleens and 2×10^6 cells were placed in V bottom 96 well plates, then labelled with fixable viability dye and then anti-B220 antibody. Subsequently, cells were stained with the cytoplasmic calcium indicator dye Fluo4-AM (Thermofisher, cat: F14201) at 10µg/ml in Iscove's Modified Dulbecco Media (IMDM) supplemented with 1% FBS at 37°C for 15 mins. Following a single wash, cells were resuspended in 400µl warm IMDM with 1% FBS. Samples were kept in a warm water container (≈37°C) throughout the flow cytometry acquisition to maintain physiologic activity. Baseline fluorescence intensity was measured for 30s prior to stimulation with either CXCL12 (200ng/ml) or anti-IgM (10µg/ml). Flow cytometry acquisition was performed on a BD Fortessa X20 at low-speed setting for 5 min, technical replicates were also included. The acquisition sequence was alternated between wild type and experimental samples in each

batch to avoid potential timing-related noise. Analyses were performed using the Kinetics module in Flow Jo software.

Lymphoma adoptive transfer

Following the manifestation of clinical signs of lymphoma, Eμ-myc mice were sacrificed and spleens were harvested. Non-B cells were depleted using Pan B cell isolation kit II (Miltenyi) to enrich lymphoma cells. 2×10^6 lymphoma cells were then intravenously injected to recipient B6.SJL.CD45.1 mice in 200μL PBS. Recipient mice were sacrificed at 3 weeks following adoptive transfer, and spleens and inguinal lymph nodes were harvested for further analyses.

Mixed bone marrow chimera generation

B6.SJL.CD45.1 recipient mice were given two doses of 5.5Gy irradiation four hours apart. Mice were then intravenously injected with 4×10^6 mixed bone marrow (BM) cells at a 1:1 ratio, isolated from age- and sex-matched CD45.2$^+$ Aicda-WT and CD45.1$^+$ WT or CD45.2$^+$ Aicda-Tfam and CD45.1$^+$ WT donor mice. Recipient mice were maintained on antibiotics (Baytril, Bayer corporation) in drinking water for two weeks. BM reconstitution was confirmed via flow cytometry of peripheral blood at 8 weeks. Mice were immunised with SRBC at 11 weeks following irradiation and analysed at Day 7.

In vitro cell culture

Daudi cells were cultured in RPMI 1640 medium supplemented with 10% FBS, 1× GlutaMAX (Gibco), 25mM HEPES and 100U/ml penicillin and 50μg/ml streptomycin and maintained at 37°C in a humidified incubator with 5% CO_2. IMT1 was ordered from MedChem Express as a 1mM stock solution in DMSO (cat no. HY-134539) and used at 0.1μM, 1μM, and 10μM concentrations for a 0-120h time window. Chloramphenicol (Merck, cat no: C0378-5G) was used at 10μg/ml and 25μg/ml concentrations (prepared in 100% ethanol fresh for each culture experiment) for a 0-120h time window. Cell numbers were determined by manual counting using Trypan blue dye for dead cell exclusion at each timepoint.

Single cell RNA-seq analysis

Approximately 17,000 cells per sample were loaded onto the 10X Genomics Chromium Controller (Chip K). Gene expression and BCR sequencing libraries were prepared using the 10x Genomics Single Cell 5' Reagent Kits v2 (Dual Index) following manufacturer user guide (CG000330 Rev B). The final libraries were diluted to ~10nM for storage. The 10nM library was denatured and further diluted prior to loading on the NovaSeq6000 sequencing platform (Illumina, v1.5 chemistry, 28bp/98bp paired end) at the Oxford Genomics Centre.

Filtered output matrices from Cellranger 6.0.1 were loaded in *Seurat* v4.1.0. Cells with more than 5% mitochondrial reads and <200 genes were removed from analysis. Data were normalised and transformed using SCTransform, with regression of cell cycle phase and mitochondrial reads, and integrated using FindIntegrationAnchors and IntegrateData functions. Principal component analysis and UMAP were used to cluster cells. Marker genes between clusters were identified using the FindAllMarkers function. Two small contaminant clusters (<1% of cells) were identified based on expression of non-B cell genes and were removed from subsequent analysis. Clusters were identified by expression of canonical

markers. Cluster proportions were calculated using *DittoSeq*. For visualisation of UMAP projections, equal number of cells from each experimental condition were displayed by random downsampling. Differential gene expression between conditions was calculated using the FindMarkers function with the 't-test' parameter. Pathway analysis was performed using *SCPA*. Pseudobulk differential gene expression between individual biological replicates was performed using *EdgeR* after count aggregation across cells using *Scuttle*.

Filtered contig outputs generated by Cellranger 6.0.1 from cells processed in the Seurat workflow above were combined, filtered, and visualised using *scRepertoire* 1.5.2. For quantification of mutational load, the *Immcantation* pipeline was employed. Germline segment assignment was performed using *Change-O*, and SHM count was calculated using *SHazaM*.

Data and code availability

Single cell RNA sequencing data has been deposited to GEO under accession number GSE208021. Code used in analysis of data is available upon reasonable request.

Acknowledgements and funding

We thank Jonathan Webber for flow sorting, Tal Arnon and Peter McGill (University of Oxford) for providing mice and Lynn Dustin (University of Oxford) for providing Daudi cells. Funding for this work was provided by the Wellcome Trust (211072/Z/18/Z), Cancer Research UK/Versus Arthritis (C70663/A29547), the Kennedy Trust for Rheumatology Research, and the US National Institutes of Health (HL118979). Flow cytometry and microscopy facilities were supported by the Kennedy Trust for Rheumatology Research through the Cell Dynamics Platform. We thank the Wolfson Imaging Centre Oxford for providing microscope facility support.

Author contributions

Y.Y. and A.C. conceived and designed the study. Y.Y. performed the majority of the experiments. E.M., E.C., S.G., C.S., and M.A. performed experiments. Y.Y. and A.C. wrote the manuscript. A.C. analysed single cell data. M.D. provided advice and guidance. A.C. supervised the study.

References

1. Young, C. & Brink, R. The unique biology of germinal center B cells. *Immunity* **54**, 1652–1664 (2021).
2. Ott, G., Rosenwald, A. & Campo, E. Understanding MYC-driven aggressive B-cell lymphomas: pathogenesis and classification. **122**, 8 (2013).
3. Victora, G. D. *et al.* Germinal Center Dynamics Revealed by Multiphoton Microscopy with a Photoactivatable Fluorescent Reporter. *Cell* **143**, 592–605 (2010).
4. Abbott, R. K. *et al.* Germinal Center Hypoxia Potentiates Immunoglobulin Class Switch Recombination. *J. Immunol.* **197**, 4014–4020 (2016).
5. Cho, S. H. *et al.* Germinal centre hypoxia and regulation of antibody qualities by a hypoxia response system. *Nature* **537**, 234–238 (2016).
6. Weisel, F. J. *et al.* Germinal center B cells selectively oxidize fatty acids for energy while conducting minimal glycolysis. *Nat. Immunol.* **21**, 331–342 (2020).

7. Boothby, M. R. *et al.* Over-Generalizing About GC (Hypoxia): Pitfalls of Limiting Breadth of Experimental Systems and Analyses in Framing Informatics Conclusions. *Front. Immunol.* **12**, 664249 (2021).
8. Chen, D. *et al.* Coupled analysis of transcriptome and BCR mutations reveals role of OXPHOS in affinity maturation. *Nat. Immunol.* 1–10 (2021) doi:10.1038/s41590-021-00936-y.
9. Haniuda, K., Fukao, S. & Kitamura, D. Metabolic Reprogramming Induces Germinal Center B Cell Differentiation through Bcl6 Locus Remodeling. *Cell Rep.* **33**, 108333 (2020).
10. Caro, P. *et al.* Metabolic Signatures Uncover Distinct Targets in Molecular Subsets of Diffuse Large B Cell Lymphoma. *Cancer Cell* **22**, 547–560 (2012).
11. Tsui, C. *et al.* Protein Kinase C-β Dictates B Cell Fate by Regulating Mitochondrial Remodeling, Metabolic Reprogramming, and Heme Biosynthesis. *Immunity* **48**, 1144-1159.e5 (2018).
12. Akkaya, M. *et al.* Second signals rescue B cells from activation-induced mitochondrial dysfunction and death. *Nat. Immunol.* **19**, 871–884 (2018).
13. Jang, K.-J. *et al.* Mitochondrial function provides instructive signals for activation-induced B-cell fates. *Nat. Commun.* **6**, 6750 (2015).
14. McWilliams, T. G. *et al.* mito-QC illuminates mitophagy and mitochondrial architecture in vivo. *J. Cell Biol.* **214**, 333–345 (2016).
15. Kennedy, D. E. *et al.* Novel specialized cell state and spatial compartments within the germinal center. *Nat. Immunol.* **21**, 660–670 (2020).
16. Martinez-Martin, N. *et al.* A switch from canonical to noncanonical autophagy shapes B cell responses. *Sci. N. Y. NY* **355**, 641–647 (2017).
17. Ott, M., Amunts, A. & Brown, A. Organization and Regulation of Mitochondrial Protein Synthesis. *Annu. Rev. Biochem.* **85**, 77–101 (2016).
18. Kaufman, B. A. *et al.* The Mitochondrial Transcription Factor TFAM Coordinates the Assembly of Multiple DNA Molecules into Nucleoid-like Structures□D. *Mol. Biol. Cell* **18**, 12 (2007).
19. Hillen, H. S., Temiakov, D. & Cramer, P. Structural basis of mitochondrial transcription. *Nat. Struct. Mol. Biol.* **25**, 754–765 (2018).
20. Brüser, C., Keller-Findeisen, J. & Jakobs, S. The TFAM-to-mtDNA ratio defines inner-cellular nucleoid populations with distinct activity levels. *Cell Rep.* **37**, 110000 (2021).
21. Baixauli, F. *et al.* Mitochondrial Respiration Controls Lysosomal Function during Inflammatory T Cell Responses. *Cell Metab.* **22**, 485–498 (2015).
22. Desdín-Micó, G. *et al.* T cells with dysfunctional mitochondria induce multimorbidity and premature senescence. *Science* **368**, 1371–1376 (2020).
23. Hobeika, E. *et al.* Testing gene function early in the B cell lineage in mb1-cre mice. *Proc. Natl. Acad. Sci. U. S. A.* **103**, 13789–13794 (2006).
24. Melchers, F. Checkpoints that control B cell development. *J. Clin. Invest.* **125**, 2203–2210 (2015).
25. Bibby, J. A. *et al.* Systematic Single Cell Pathway Analysis (SCPA) reveals novel pathways engaged during early T cell activation. 42.
26. Shaulian, E. & Karin, M. AP-1 as a regulator of cell life and death. *Nat. Cell Biol.* **4**, E131–E136 (2002).
27. Suzuki, Y. J., Forman, H. J. & Sevanian, A. Oxidants as Stimulators of Signal Transduction. *Free Radic. Biol. Med.* **22**, 269–285 (1997).
28. Ansel, K. M., Harris, R. B. S. & Cyster, J. G. CXCL13 is required for B1 cell homing, natural antibody production, and body cavity immunity. *Immunity* **16**, 67–76 (2002).
29. Han, S.-B. *et al.* Rgs1 and Gnai2 Regulate the Entrance of B Lymphocytes into Lymph Nodes and B Cell Motility within Lymph Node Follicles. *Immunity* **22**, 343–354 (2005).

30. Föger, N., Rangell, L., Danilenko, D. M. & Chan, A. C. Requirement for Coronin 1 in T Lymphocyte Trafficking and Cellular Homeostasis. *Science* **313**, 839–842 (2006).
31. Bolger-Munro, M. *et al.* Arp2/3 complex-driven spatial patterning of the BCR enhances immune synapse formation, BCR signaling and B cell activation. *eLife* **8**, e44574 (2019).
32. West, A. P. *et al.* Mitochondrial DNA stress primes the antiviral innate immune response. *Nature* **520**, 553–557 (2015).
33. Argüello, R. J. *et al.* SCENITH: A Flow Cytometry-Based Method to Functionally Profile Energy Metabolism with Single-Cell Resolution. *Cell Metab.* **32**, 1063-1075.e7 (2020).
34. Allen, C. D. C. *et al.* Germinal center dark and light zone organization is mediated by CXCR4 and CXCR5. *Nat. Immunol.* **5**, 943–952 (2004).
35. Tolar, P. Cytoskeletal control of B cell responses to antigens. *Nat. Rev. Immunol.* **17**, 621–634 (2017).
36. Maus, M. *et al.* B cell receptor-induced Ca^{2+} mobilization mediates F-actin rearrangements and is indispensable for adhesion and spreading of B lymphocytes. *J. Leukoc. Biol.* **93**, 537–547 (2013).
37. Williams, G. S. B., Boyman, L., Chikando, A. C., Khairallah, R. J. & Lederer, W. J. Mitochondrial calcium uptake. *Proc. Natl. Acad. Sci.* **110**, 10479–10486 (2013).
38. Li, F. *et al.* Myc Stimulates Nuclearly Encoded Mitochondrial Genes and Mitochondrial Biogenesis. *Mol. Cell. Biol.* **25**, 6225–6234 (2005).
39. Harris, A. W. *et al.* The E mu-myc transgenic mouse. A model for high-incidence spontaneous lymphoma and leukemia of early B cells. *J. Exp. Med.* **167**, 353–371 (1988).
40. Bonekamp, N. A. *et al.* Small-molecule inhibitors of human mitochondrial DNA transcription. *Nature* **588**, 712–716 (2020).
41. McKee, E. E., Ferguson, M., Bentley, A. T. & Marks, T. A. Inhibition of Mammalian Mitochondrial Protein Synthesis by Oxazolidinones. *Antimicrob. Agents Chemother.* **50**, 2042–2049 (2006).
42. Waters, L. R., Ahsan, F. M., Wolf, D. M., Shirihai, O. & Teitell, M. A. Initial B Cell Activation Induces Metabolic Reprogramming and Mitochondrial Remodeling. *ISCIENCE* **5**, 99–109 (2018).
43. Oestreich, K. J. *et al.* Bcl-6 directly represses the gene program of the glycolysis pathway. *Nat. Immunol.* **15**, 957–964 (2014).
44. Campello, S. *et al.* Orchestration of lymphocyte chemotaxis by mitochondrial dynamics. *J. Exp. Med.* **203**, 2879–2886 (2006).
45. Klemke, M. *et al.* Oxidation of Cofilin Mediates T Cell Hyporesponsiveness under Oxidative Stress Conditions. *Immunity* **29**, 404–413 (2008).
46. D'Andrea, A. *et al.* The mitochondrial translation machinery as a therapeutic target in Myc-driven lymphomas. *Oncotarget* **7**, 72415–72430 (2016).
47. Dominguez-Sola, D. *et al.* The FOXO1 Transcription Factor Instructs the Germinal Center Dark Zone Program. *Immunity* **43**, 1064–1074 (2015).
48. Cato, M. H., Yau, I. W. & Rickert, R. C. Magnetic-based purification of untouched mouse germinal center B cells for ex vivo manipulation and biochemical analysis. *Nat. Protoc.* **6**, 953–960 (2011).
49. Yazicioglu, Y. F., Aksoylar, H. I., Pal, R., Patsoukis, N. & Boussiotis, V. A. Unraveling Key Players of Humoral Immunity: Advanced and Optimized Lymphocyte Isolation Protocol from Murine Peyer's Patches. *J. Vis. Exp.* e58490 (2018) doi:10.3791/58490.
50. Ollion, J., Cochennec, J., Loll, F., Escudé, C. & Boudier, T. TANGO: a generic tool for high-throughput 3D image analysis for studying nuclear organization. *Bioinformatics* **29**, 1840–1841 (2013).

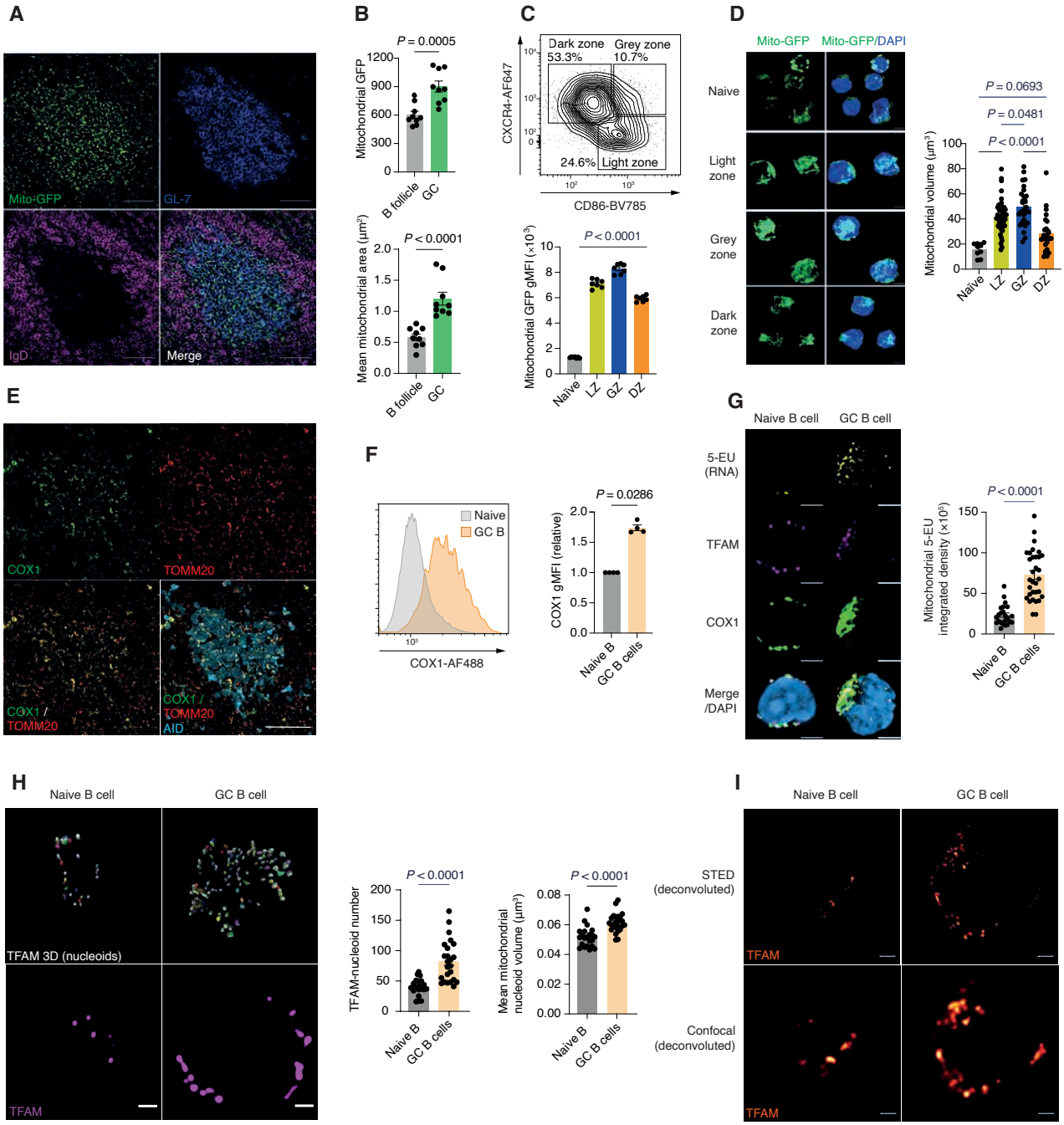

Figure 1. GC B cells undergo extensive mitochondrial remodelling and biogenesis associated with mitochondrial protein translation

A. Spleen sections from MitoQC mice immunised with SRBC and analysed at D12. Scale bar 50µm. Representative of two independent experiments

B. Quantification of mitochondrial GFP signal intensity and area (µm²) in GCs. Each point represents an individual GC, pooled from three individual MitoQC mice immunised as in A. Representative of two independent experiments.

C. Gating strategy for GC B cells and their subsets in the spleen. GC and naïve B cells were gated as $CD19^{+}CD38^{-}GL\text{-}7^{+}$ and $CD19^{+}IgD^{+}GL\text{-}7^{-}$ respectively. GC B cells from the dark zone (DZ), grey zone (GZ), and light zone (LZ) were identified based on CXCR4 and CD86 expression signatures as depicted. Quantification and comparison of gMFI of mitochondrial GFP in splenic naïve, LZ, GZ and DZ GC B cells from immunised MitoQC mice (n=7), pooled from two independent experiments.

D. 3D Airyscan immunocytochemistry (ICC) images depicting the mitochondrial network (GFP) in MACS-enriched and flow sorted GC B cells (LZ, GZ, and DZ) and magnetic bead sorted naïve B cells harvested from immunised (enhanced SRBC immunisation protocol at D12) and unimmunised MitoQC spleens, scale bar 3µm. 3D mitochondrial volume (μm^3) quantification in naïve, LZ, GZ, and DZ compartments, isolated as in D. Each symbol represents one cell.
E. Spleen sections from Aicda-Cre × Rosa26^{STOP}tdTomato mice immunised with SRBC and analysed at D12, with IHC for COX1 and TOMM20. Scale bar 50µm. Representative of two independent experiments.
F. Flow cytometry histogram plots and quantification of COX1 protein levels in GC B cells normalised to IgD$^+$ naïve B cells (n=4). Representative of three independent experiments.
G. Airyscan images of in vivo 5-EU incorporation (indicating RNA synthesis), with COX1 and TFAM ICC in naïve and GC B cells. Quantification of mitochondrial 5-EU integrated signal density in naïve and GC B cells following ex vivo incorporation. Scale bar 3µm.
H. 2D Airyscan ICC images of TFAM in naïve and GC B cells, with 3D reconstruction indicating individual mitochondrial nucleoids. Quantification of nucleoid number and volume. Each symbol represents one cell. Scale bar 1µm. Representative of two independent experiments
I. Deconvoluted confocal and STED super-resolution ICC images of TFAM in naïve and GC B cells. Scale bar 1µm.

Statistical significance was calculated by unpaired two-tailed t-test (B, G, H), Mann Whitney U test (F) or ordinary one-way ANOVA with Tukey's multiple comparisons test (C, D)

Figure 2

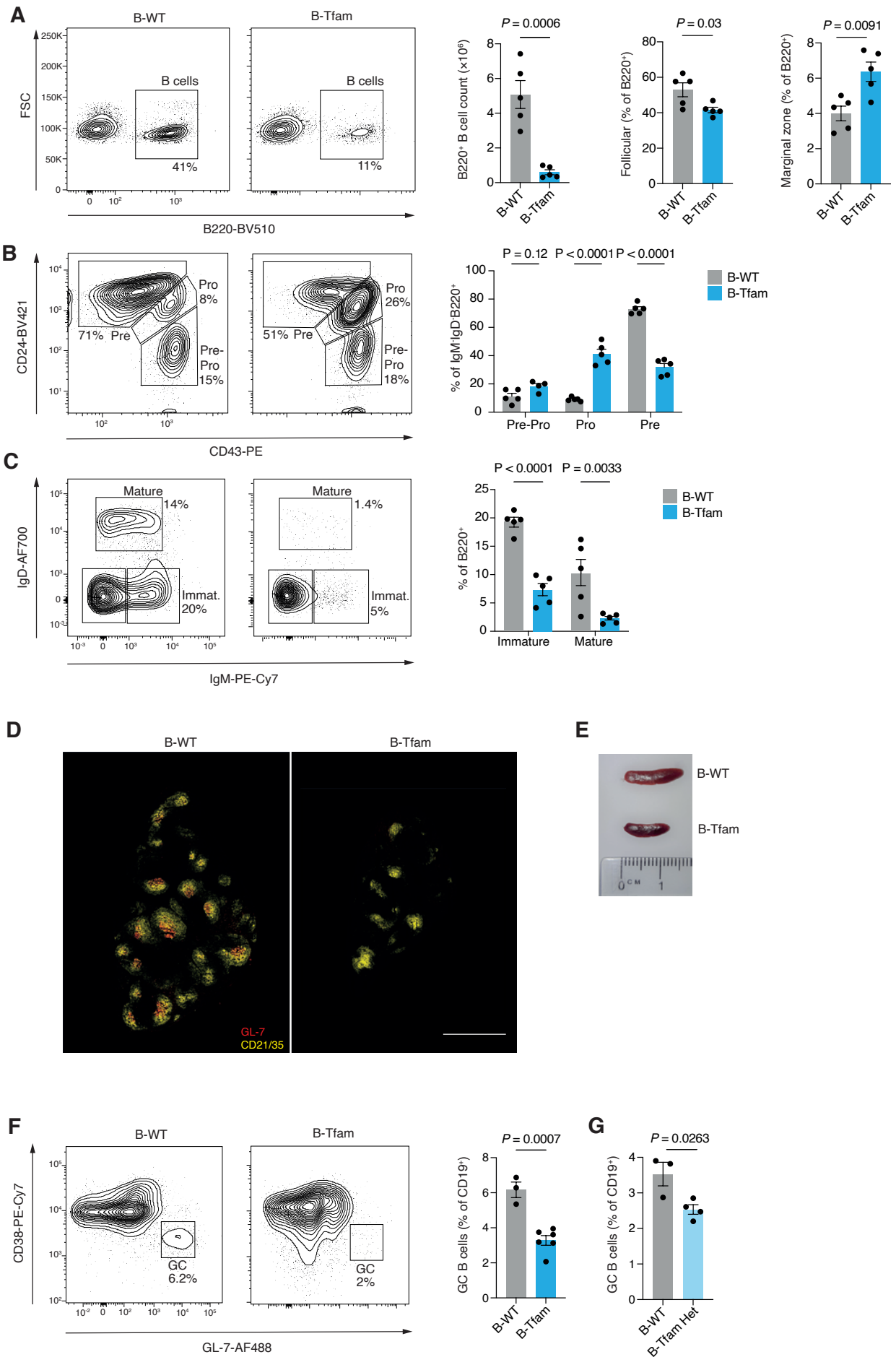

Figure 2. *Tfam* is essential for B cell development and differentiation

A. Representative flow cytometry plots of $B220^+$ B cells from the spleens of 6-week-old B-Tfam and B-WT mice, with quantification of total splenic B cell counts, and proportions of follicular ($CD23^+CD21^-$) and marginal zone ($CD21^+CD23^-$) B cell subsets (n=5). Representative of two independent experiments.

B. Representative flow cytometry plots and quantification of bone marrow $IgM^-IgD^-B220^+$ pre-pro, pro and pre-B cells isolated from B-Tfam and B-WT mice (n=5). Results representative of two independent experiments.

C. Representative flow cytometry plots and quantification of bone marrow-resident $B220^+$ IgM^+IgD^- immature and $B220^+IgD^+$ mature B cell subsets from B-WT and B-Tfam mice (n=5). Results representative of two independent experiments.

(D-G) B-WT and B-Tfam mice were immunised with SRBCs (day 0 & 5) intraperitoneally, and at day 12 spleens were analysed by flow cytometry and immunohistochemistry (IHC)

D. Representative tile-scan images of spleen sections from B-Tfam and B-WT mice depicting $GL\text{-}7^+$ GCs and $CD21/35^+$ B cell follicles. Scale bar 500µm.

E. Representative images of spleens from littermate B-Tfam and B-WT mice.

F. Flow cytometry gating strategy and quantification of $CD38^-GL\text{-}7^+$ GC B cells in spleens of immunised B-Tfam (n=6) and B-WT mice (n=3). Results representative of two independent experiments.

G. Comparison of $CD38^-GL\text{-}7^+$ GC B cell proportions in spleens of SRBC-immunised B-Tfam Het (Cd79a-Cre × Tfam $^{flox/+}$)(n=4) and B-WT mice (n=3). Results representative of two independent experiments.

Statistical significance was calculated by two-way ANOVA with Šidák's multiple comparison (B, C) or unpaired two-tailed t-test (A, F, G)

Figure 3

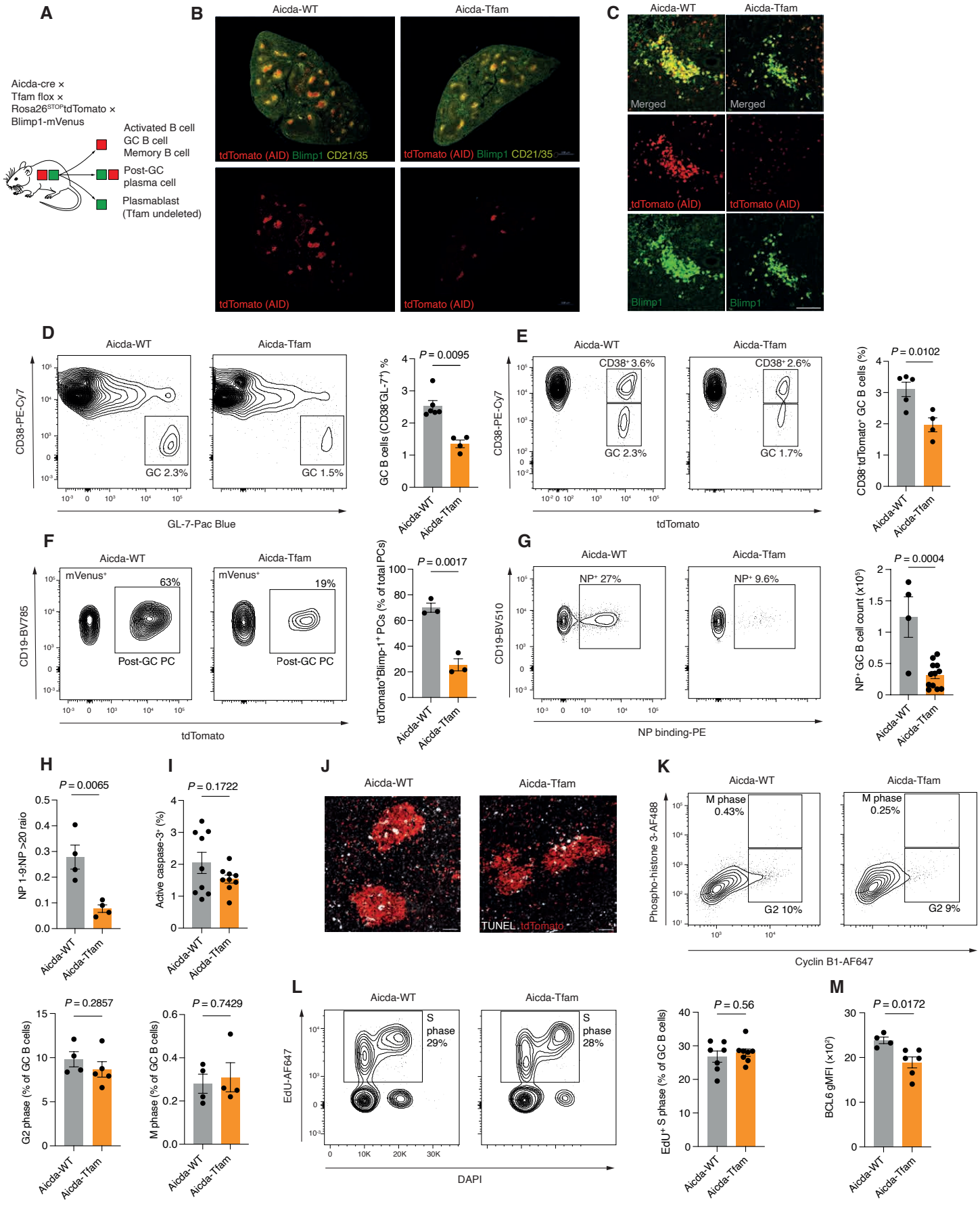

Figure 3. GC B cells require TFAM

A. Schematic of Aicda-Tfam mouse (Aicda-cre × Tfam flox × Rosa26^{STOP}tdTomato × Blimp1-mVenus)

(B-F) Aicda-WT and Aicda-Tfam mice were immunised with SRBCs intraperitoneally, and on day 12 spleens were analysed by flow cytometry and/or immunohistochemistry (IHC)

B. Representative IHC images of spleen sections from Aicda-Tfam and Aicda-WT mice. Scale bar 500µm. Representative of three independent experiments

C. Airyscan images of plasma cell clusters in red pulp of spleen sections. tdTomato$^+$Blimp1-mVenus$^+$ double positive cells indicate post-GC plasma cells. Scale bar 75µm.

D. Representative flow cytometry plots for the identification of GC B cells from Aicda-WT (n=6) and Aicda-Tfam (n=4) mice following SRBC immunisation. Quantification of CD38$^-$GL-7$^+$ GC B cell percentages within the CD19$^+$ B cell compartment. Representative of four independent experiments.

E. Representative flow cytometry plots for the identification of GC B cells as CD38$^-$tdTomato$^+$ in Aicda-WT (n=5) and Aicda-Tfam (n=4) mice. Results representative of four independent experiments.

F. Representative flow cytometry plots depicting tdTomato$^+$ Blimp1-mVenus$^+$ post-GC plasma cells within the Dump$^-$mVenus-Blimp1$^+$ cell compartment. Comparison of tdTomato$^+$ proportion within Dump$^-$mVenus-Blimp1$^+$ PC compartment (n=3). Data representative of four independent experiments.

(G-K) Aicda-WT and Aicda-Tfam mice were immunised with 50µg NP-CGG with Alum (at 1:1 ratio) intraperitoneally, and on day 14 spleens were harvested for flow cytometry and IHC analyses.

G. Representative flow cytometry plots depicting CD19$^+$CD38$^-$GL-7$^+$ GC B cells binding NP-PE or -APC from Aicda-Tfam (n=8) or Aicda-WT (n=9). Quantification of NP-specific GC B cells. Data pooled from and representative of three independent experiments.

H. ELISA quantification and comparison of the ratio of NP-specific high-affinity antibodies to low-affinity antibodies detected by binding to $NP_{1\text{-}9}$ and $NP_{>20}$ antigens respectively from Aicda-WT (n=4) and Aicda-Tfam (n=4). Data representative of two independent experiments.

I. Quantification of active (cleaved) caspase 3$^+$ apoptotic GC B cells as a percentage of total GC B cells (n=9). Data pooled from two independent experiments.

J. IHC images of in situ TUNEL assay on Aicda-WT and Aicda-Tfam spleens. Scale bar 50 µm. Representative of two independent replicates

K. Representative flow cytometry plots depicting identification of M and G2 cell cycle stages in GC B cells from Aicda-WT and Aicda-Tfam mice (n=4), based on phospho-histone 3 and cyclin B1 expression. Data representative of two independent experiments.

L. Representative flow cytometry plots depicting identification of S phase cell cycle stage in GC B cells from Aicda-WT and Aicda-Tfam mice, based on EdU and DAPI uptake (n=7). Data representative of two independent experiments.

M. Quantification of BCL6 expression in GC B cells from Aicda-WT and Aicda-Tfam mice (n=4). Data representative of two independent experiments.

Statistical significance was calculated by unpaired two-tailed t-test (D-I, K-M).

Figure 4

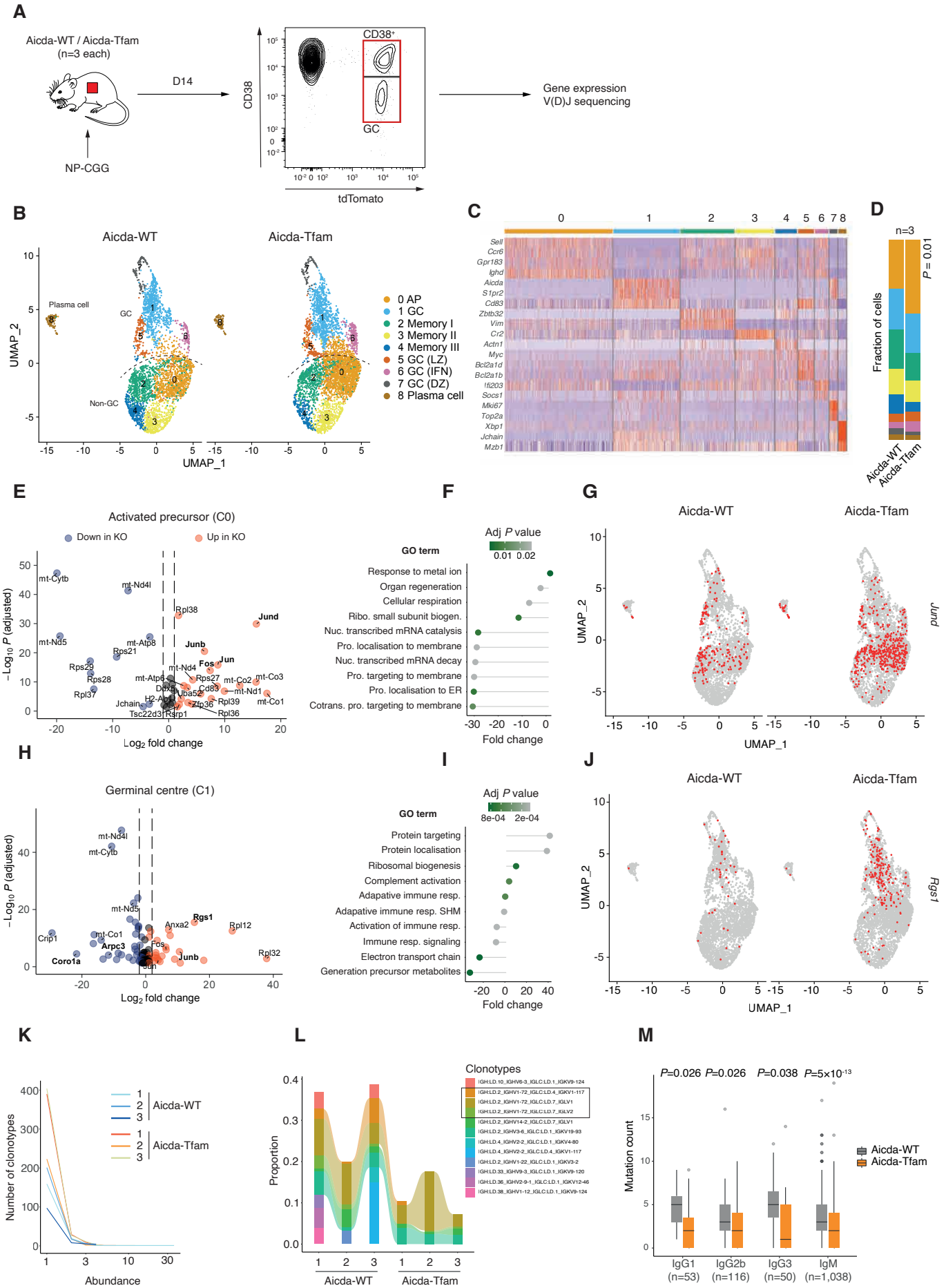

Figure 4. TFAM controls transcriptional entry into the GC program

A. Schematic of experimental design. Aicda-WT and Aicda-Tfam mice (n=3 per group) were immunised with 50µg NP-CGG with Alum (at 1:1 ratio) intraperitoneally and Dump$^-$ CD19$^+$tdTomato$^+$ cells were flow sorted before bead capture and 10x library preparation and sequencing.
B. UMAP projections and clustering of integrated Aicda-WT and Aicda-Tfam datasets.
C. Heatmap of selected differentially expressed marker genes by cluster for all samples.
D. Cluster proportions between groups.
E. Volcano plot of differentially expressed genes in cluster 0 (activated precursors).
F. Single cell pathway analysis (SCPA) of Gene Ontogeny Biologicals Processes (GO BP) in AP cluster.
G. *Jund* gene expression projected onto clustered data.
H. Volcano plot of differentially expressed genes in cluster 1 (germinal centre).
I. SCPA of GO BP in germinal centre cluster (cluster 1).
J. *Rgs1* gene expression projected onto clustered data.
K. Plot of clonotype abundance distribution for each sample.
L. Plot of proportions of top clonotypes for each sample. Clonotypes with *Ighv1-72* usage are highlighted.
M. Quantification of somatic hypermutation by mutation count for each immunoglobulin isotype.

Statistical significance was calculated by t-test with correction for multiple comparison by Bonferroni (E, H) or Benjamini-Hochberg (M) methods.

Figure 5

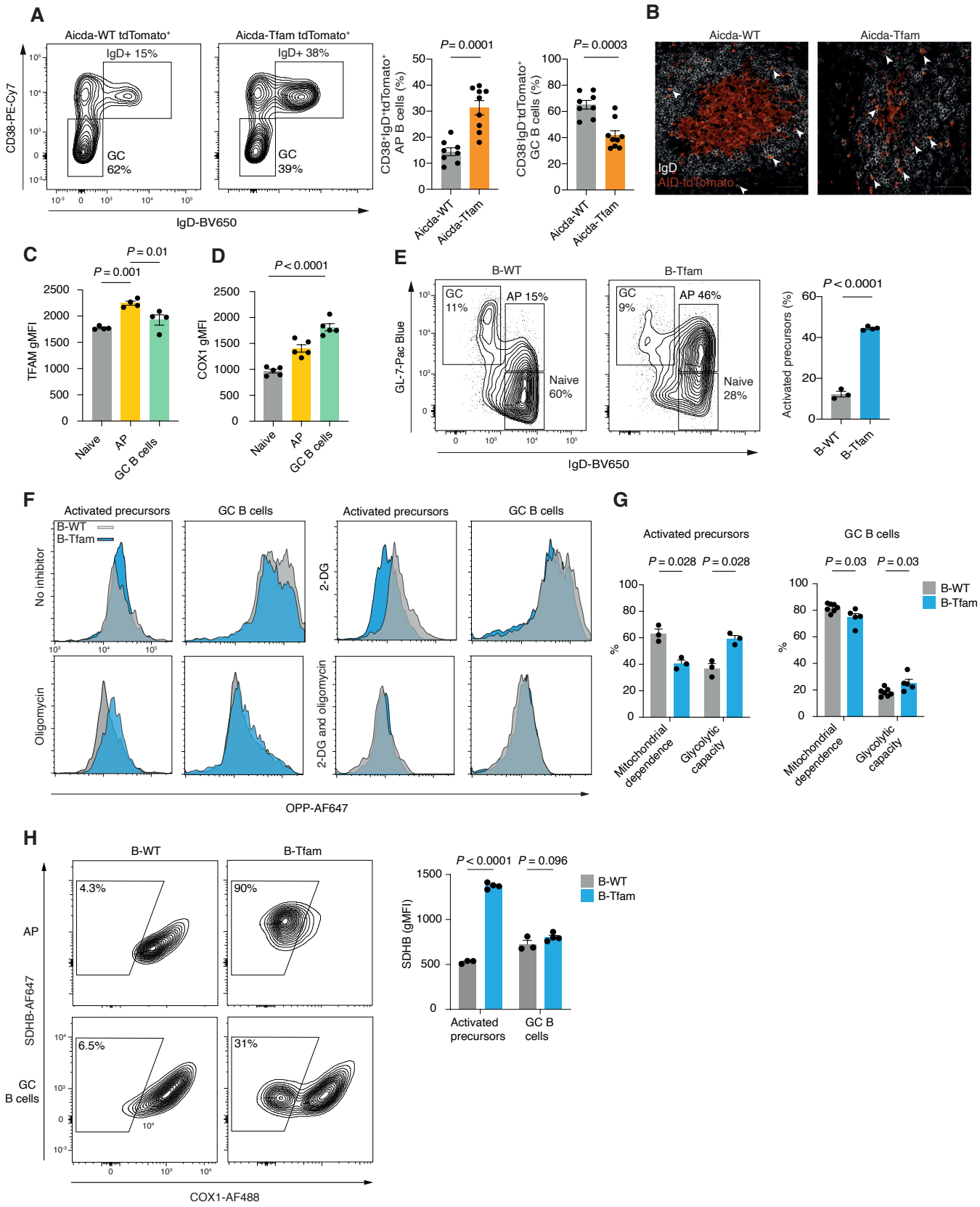

Figure 5. TFAM is required for GC B cell commitment

A. Representative flow cytometry plots depicting gating of $CD38^{+}IgD^{+}$ activated precursors (AP) and $CD38^{-}IgD^{-}$ GC B cells within the $CD19^{+}tdTomato^{+}$ population. Quantification of AP and GC B cell percentages from NP-CGG immunised Aicda-WT (n=8) and Aicda-Tfam mice (n=9). Data pooled from two independent experiments

B. Representative IHC images of GCs from Aicda-WT and Aicda-Tfam mice. Arrows identify $tdTomato^{+}IgD^{+}$ APs. 20× magnification, scale bar 20μm. Representative of two independent experiments. Quantification of TFAM gMFI in $tdTomato^{+}CD38^{-}$ GC B cells, $tdTomato^{+}IgD^{+}$ AP, and $tdTomato^{-}IgD^{+}$ naïve B cell compartments from SRBC immunised Aicda-WT and Aicda-Tfam mice (n=5). Data representative of three independent experiments.

C. Quantification of TFAM gMFI in $tdTomato^{+}CD38^{-}$ GC B cells, $tdTomato^{+}IgD^{+}$ AP, and $tdTomato^{-}IgD^{+}$ naïve B cell compartments from SRBC immunised Aicda-WT and Aicda-Tfam mice (n=5). Data representative of three independent experiments.

D. Quantification of COX1 gMFI in $tdTomato^{+}CD38^{-}$ GC B cells, $tdTomato^{+}IgD^{+}$ AP, and $tdTomato^{-}IgD^{+}$ naïve B cell compartments from SRBC immunised Aicda-WT and Aicda-Tfam mice (n=5). Data representative of three independent experiments.

E. Representative flow cytometry plots depicting $IgD^{+}GL\text{-}7^{int}$ AP and $IgD^{-}GL\text{-}7^{+}$ GC B cell subsets in B-WT and B-Tfam mice immunised with SRBC (enhanced protocol). Quantification and comparison of $IgD^{+}GL\text{-}7^{+}$ AP proportions in B-WT (n=3) and B-Tfam mice (n=4). Data representative of three independent experiments.

F. Histogram plots depicting O-propargyl-puromycin (OPP) incorporation in splenic $IgD^{+}GL\text{-}7^{int}$ AP and $IgD^{-}GL\text{-}7^{+}CD38^{-}$ GC B cells from B-WT (n=3) and B-Tfam mice (n=3), treated ex vivo with metabolic inhibitors (oligomycin and/or 2-DG). Data representative of or pooled from two independent experiments.

G. Quantification of mitochondrial dependence and glycolytic capacity of cells from (F).

Statistical significance was calculated by unpaired two-tailed t-test (A, C-E, I) or two-way ANOVA with Šidák's multiple comparison test (G-H).

Figure 6

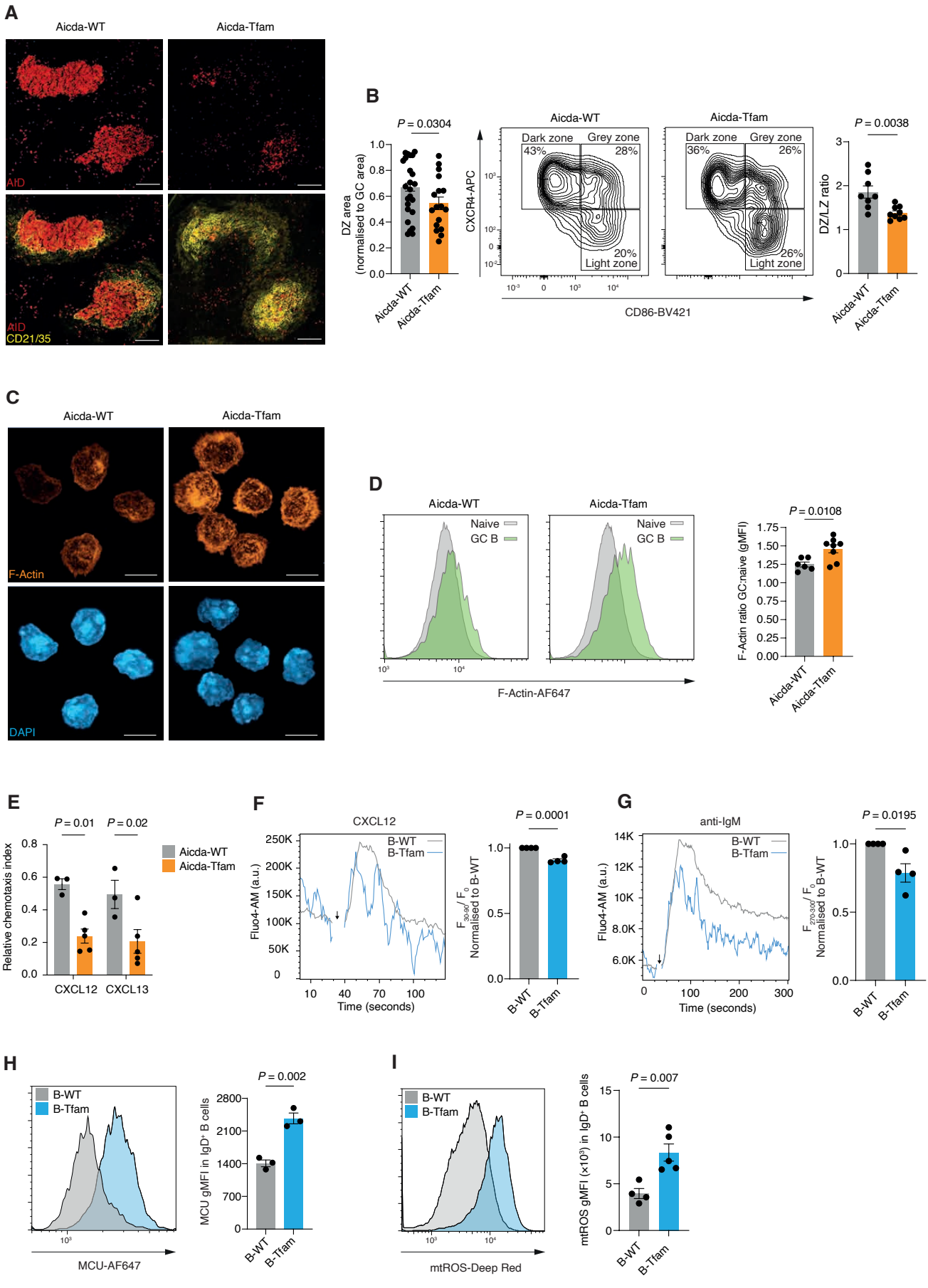

Figure 6. Tfam deletion disrupts GC spatial organisation and impairs cell mobility

A. Representative Airyscan IHC images of spleen sections from SRBC-immunised Aicda-WT and Aicda-Tfam mice. Quantification of DZ area normalised to GC area. Each symbol represents an individual GC. Image analyses were performed including all GCs identified on two sections from 2 mice of each genotype. Scale bar 100µm. Representative of >3 independent experiments.
B. Representative flow cytometry plots of DZ, GZ, and LZ subpopulations of tdTomato$^+$CD38$^-$ GL-7$^+$ GC B cells, based on CXCR4 and CD86 expression. Quantification of the DZ to LZ ratio from NP-CGG immunised Aicda-WT (n=8) and Aicda-Tfam mice (n=9). Representative of four independent experiments.
C. 3D Airyscan confocal image of magnetic bead-sorted and F-actin phalloidin and DAPI-stained GC B cells from Aicda-WT and Aicda-Tfam mice. All cells imaged expressed tdTomato. Scale bar 6µm.
D. Representative flow cytometry histogram of F-actin phalloidin fluorescence of tdTomato$^+$GL-7$^+$ GC B cells and tdTomato$^-$IgD$^+$ naïve B cells from immunised Aicda-WT (n=6) and Aicda-Tfam mice (n=8). Quantification of F-actin phalloidin gMFI in tdTomato$^+$IgD$^-$GL-7$^+$ GC B cells from immunised Aicda-WT and Aicda Tfam mice normalised to tdTomato$^-$IgD$^+$ naïve B cells. Data pooled from three independent experiments.
E. Quantification of chemotaxis to CXCL12 and CXCL13 in GC B cells from Aicda-WT and Aicda-Tfam mice (n=4). Data representative of four independent experiments.
F. Representative Fluo4-AM geometric mean signal intensity kinetics (moving average) of B-WT and B-Tfam B220$^+$ B cells stimulated with CXCL12 (200ng/ml) for 120s. Quantification of fold change in geometric MFI between 30-90s (corresponding to peak response) normalised to baseline (F_0, 0-30s pre-stimulation). Experiment was run as technical duplicates in four independent replicate experiments consisting of one B-Tfam and one wild-type mouse. Data points from B-Tfam were normalised to wild-type data run in the same batch.
G. Representative Fluo4-AM gMFI signal kinetics (moving average) of B-WT and B-Tfam B220$^+$ B cells stimulated with anti-IgM (10µg/ml) for 300s. Quantification of fold change in geometric MFI between 270-300s (corresponding to 5 min response) normalised to baseline (F_0, 0-30s). Experiment was run as technical duplicates in four independent replicate experiments consisting of one B-Tfam and one wild-type mouse in each. Data points from B-Tfam were normalised to wild-type data run in the same batch.
H. Representative flow cytometry histogram of MCU fluorescence in B220$^+$ IgD$^+$ B cells from unimmunised B-Tfam and B-WT mice. Quantification of MCU gMFI in IgD$^+$ B cells from B-Tfam and B-WT mice. Data representative of 3 independent experiments.
I. Representative flow cytometry histogram of mtROS Deep Red fluorescence in IgD$^+$ B cells from immunised B-WT (n=4) and B-Tfam mice (n=5). Data representative of two independent experiments.

Statistical significance was calculated by unpaired two-tailed t-test (B,D, F-I) or two-way ANOVA with Šidák's multiple comparison test (E).

Figure 7

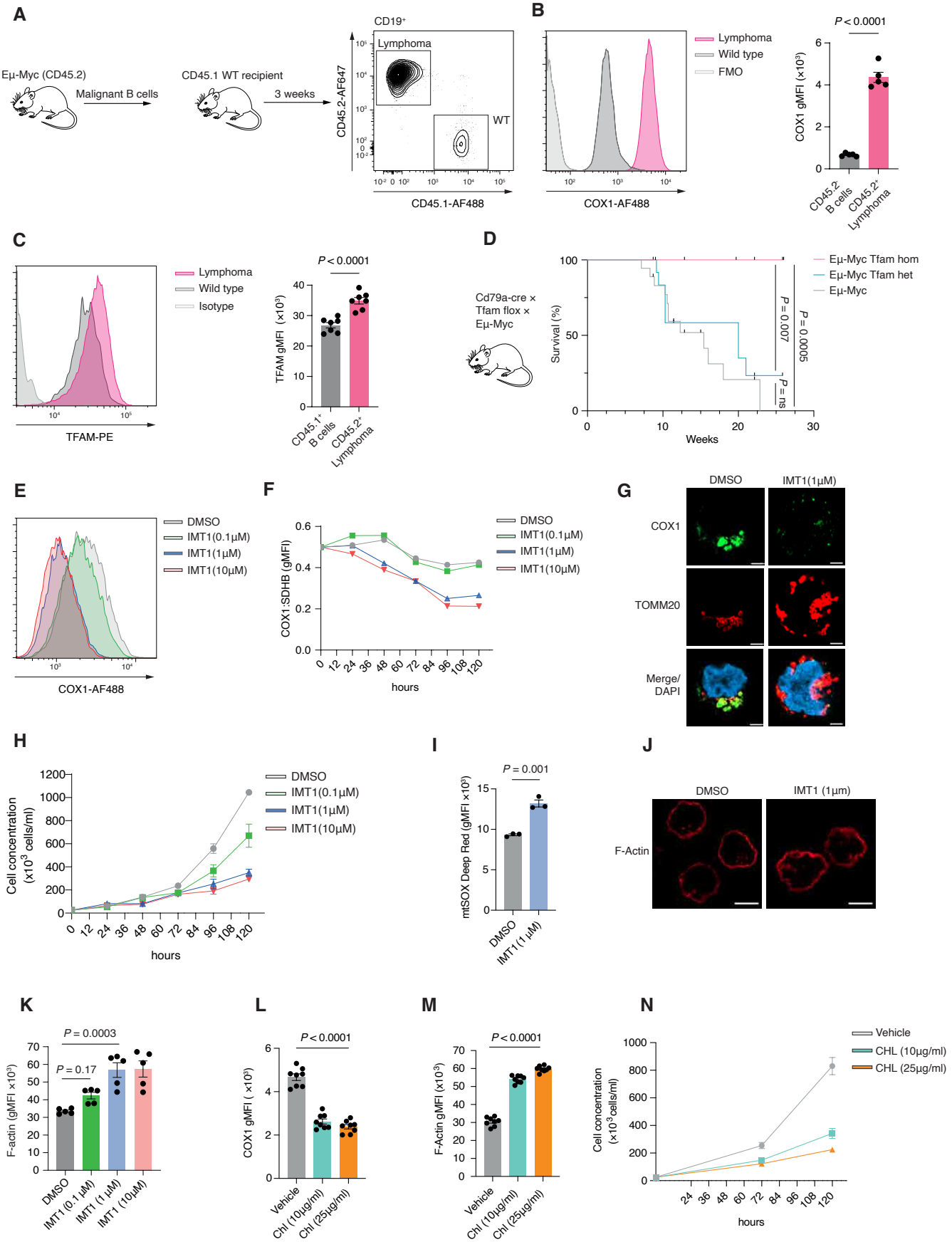

Figure 7. *Tfam* deletion in B cells abrogates the development and progression of lymphoma

A. Schematic depicting adoptive transfer strategy of lymphoma cells from Eμ-Myc mice. Following development of lymphoma, cells were transferred into wild type congenic ($CD45.1^+$) recipients. Representative flow cytometry plots showing identification of $CD19^+CD45.2^+$ donor lymphoma cells and $CD19^+CD45.1^+$ wild type B cells from the inguinal lymph nodes of recipient mice after 3 weeks.
B. Flow cytometry histogram depicting COX1 expression in $CD45.2^+$ lymphoma cells and $CD45.2^-$ wild type B cells as described in A. Quantification of COX1 gMFI. Data representative of two independent experiments.
C. Flow cytometry histogram depicting TFAM expression in $CD45.2^+$ lymphoma cells and $CD45.1^+$ WT B cells as described in A. Quantification of TFAM gMFI. Data representative of two independent experiments.
D. Kaplan-Meier graph depicting survival curve of Eμ-Myc × Tfam Hom ($Cd79a^{cre/+}$ $Tfam^{fl/fl}$ × Eμ-Myc, n=9), Eμ-Myc Tfam Het ($Cd79a^{cre/+}$ $Tfam^{fl/+}$ × Eμ-Myc, n=13) and Eμ-Myc ($Cd79a^{+/+}$ $Tfam^{fl/fl}$ × Eμ-Myc or $Cd79a^{+/+}$ $Tfam^{fl/+}$ × Eμ-Myc, n=18) mice followed for up to 6 months of age.
E. Representative flow cytometry histogram depicting COX1 expression in Daudi cell line treated with IMT1 at various concentrations (0.1μM, 1μM, 10μM) or vehicle (DMSO) for 120 hours. Representative of three independent experiments.
F. Quantification of COX1 levels by flow cytometry, normalised to SDHB in IMT1 or vehicle-treated Daudi cells at different time points (0, 24, 48, 72, 96, 120 hours), representative of two independent experiments.
G. Airyscan ICC images of COX1 and TOMM20 in Daudi cells treated with DMSO or IMT1 (1μM) for 120 hours. Scale bar 3μm.
H. Quantification of Daudi cell concentrations over 120h incubation period in the presence of IMT1 or vehicle, representative of two independent experiments with three technical replicates each.
I. Flow cytometry-based quantification of mitochondrial ROS in Daudi cell line treated with IMT1 (1μM) or vehicle (DMSO) for 120 hours.
J. Airyscan images of Daudi cells treated with IMT1 1μM or DMSO, and stained for F-actin phalloidin. Scale bar 3μm.
K. Quantification of F-actin-phalloidin fluorescence by flow cytometry, as in **J**. Each point represents one technical replicate, pooled from two independent experiments.
L. Quantification of COX1 levels in Daudi cells by flow cytometry following treatment with vehicle (ethanol) or chloramphenicol at 10μg/ml or 25μg/ml for 120 hours.
M. Quantification of F-actin levels in Daudi cells by flow cytometry following treatment with vehicle (ethanol) or chloramphenicol at 10μg/ml or 25μg/ml for 120 hours.
N. Quantification of Daudi cell concentrations over 120 hour incubation period in the presence of chloramphenicol or vehicle as in M**.** Representative of two independent experiments with four technical replicates.

Statistical significance was calculated by unpaired two-tailed t-test (B,C), Mantel-Cox log-rank test (D), two-way ANOVA with Šidák's multiple comparison test (E, F), or ordinary one-way ANOVA with Dunnett's multiple comparison test (H, J, L)

Supplementary figure 1

S1A

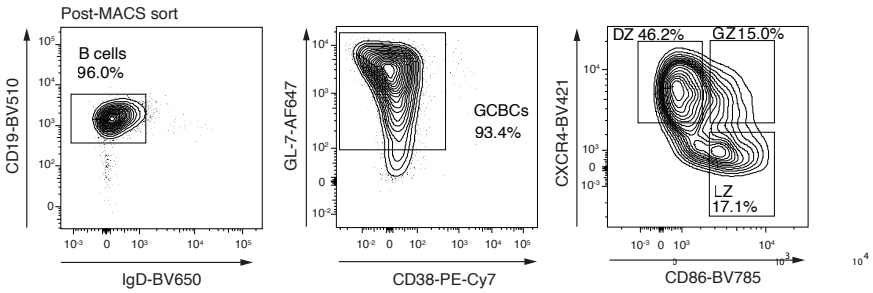

S1B

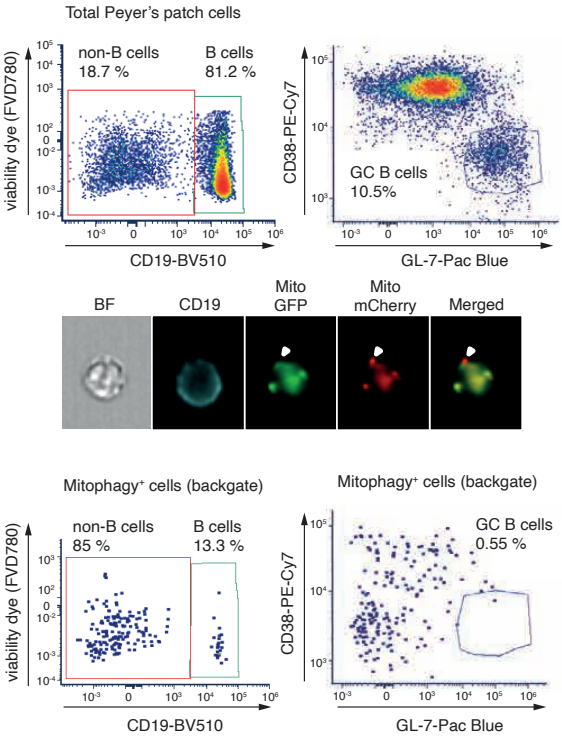

S1C

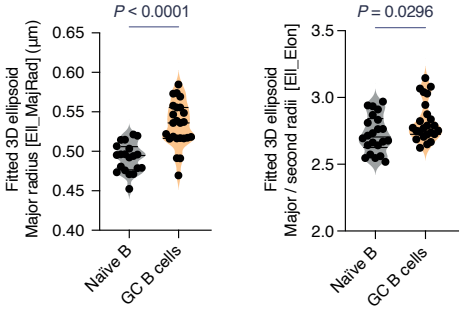

S1

A. Flow cytometry gating strategy for DZ, LZ, and GZ from MACS-enriched GC B cells isolated from SRBC-immunised (enhanced protocol, D12) MitoQC mice.
B. ImageStream gating strategy for Peyer's patch total B cells and GC B cells from unimmunised MitoQC mice. Representative image of mitophagy. Representative proportions of B cell subsets in pre-gated mitophagy⁺ population. Mitophagy was defined as the presence of foci of tdTomato signal in the absence of GFP co-localisation.
C. Quantification of average major radius and aspect ratio (major radius/second radius) of mitochondrial nucleoids based on 3D fitted ellipsoid volume model.

Statistical significance was calculated by unpaired two-tailed t-test (C).

Supplementary figure 2

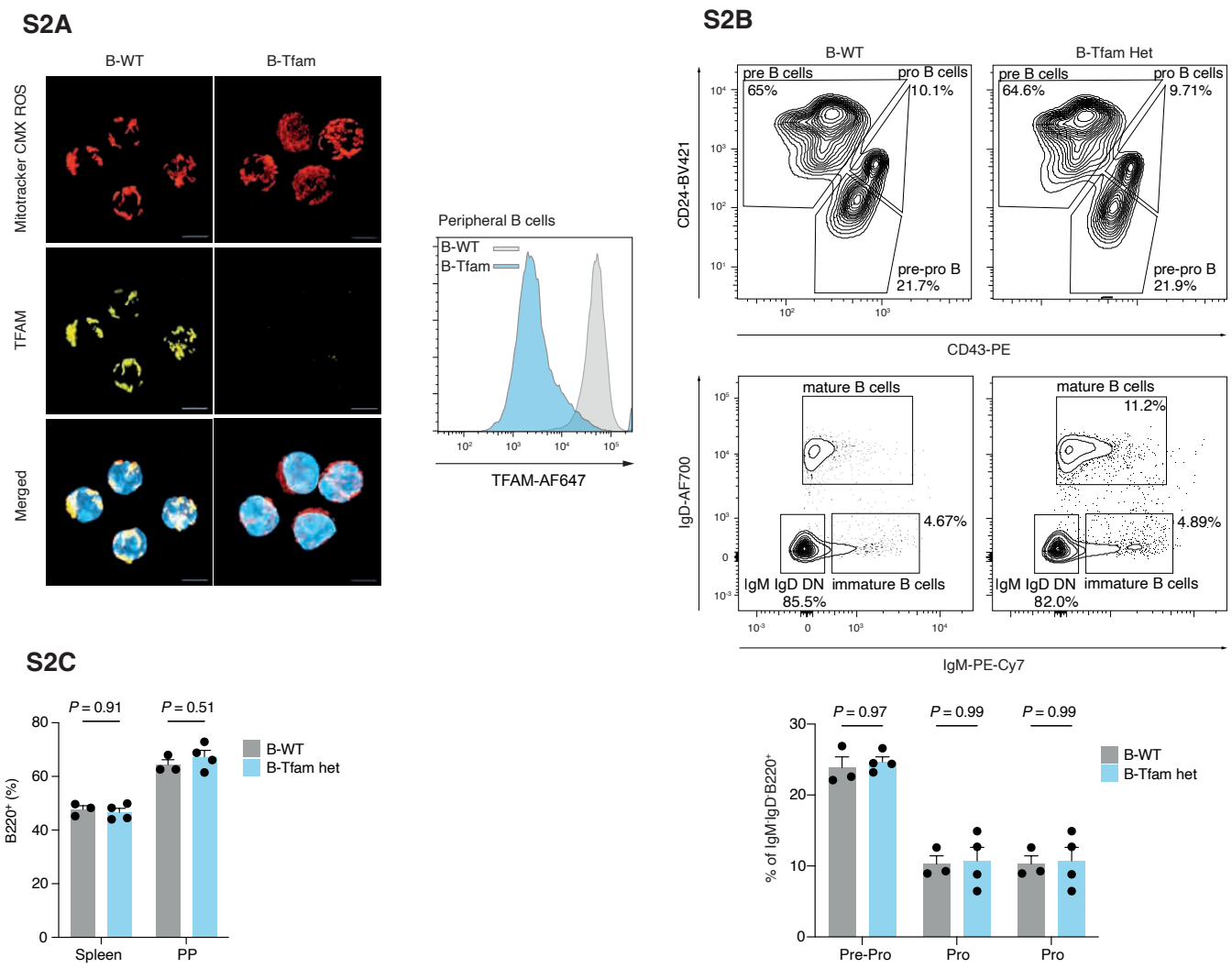

S2

A. Airyscan ICC of B cells from unimmunised B-WT and B-Tfam mice, stained for TFAM and with MitoTracker CMX ROS. FACS histogram of TFAM staining in splenic CD19⁺ B cells from unimmunised B-WT and B-Tfam mice. Scale bar = 3μm.

B. Representative flow cytometry plots of bone marrow B cell development in B-WT (n=3) and B-Tfam heterozygous mice (n=4), with quantification of pre-pro-, pro-, and pre-B cell populations, as described in figure 2B.

C. Proportional comparison of B cells in spleen and Peyer's patches from B-WT (n=3) and B-Tfam heterozygous mice (n=4). Representative of three independent experiments.

Statistical significance was calculated by two-way ANOVA with Šidák's multiple comparison test (S2B-C).

Supplementary figure 3

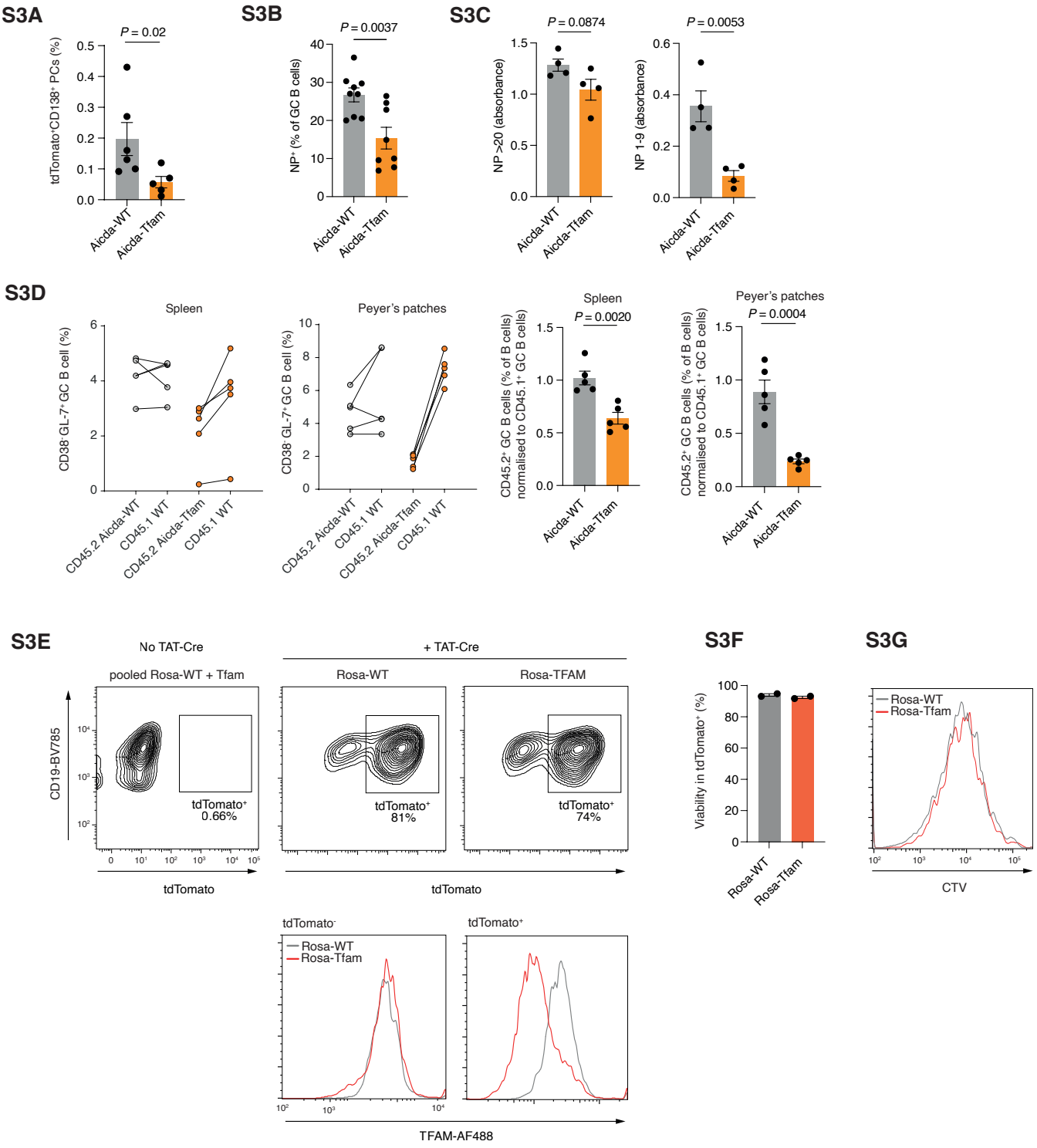

S3

A. Quantification of tdTomato+CD138+ plasma cells inbone marrow, expressed as a percentage of IgD-Dump-, in Aicda-WT and Aicda-Tfam mice immunised with SRBC and analysed at D12. Data representative of two independent experiments.

B. Quantification of NP-PE or NP-APC-binding CD19+CD38-GL-7+ GC B cell proportions in NP-CGG-immunised Aicda-WT and Aicda-Tfam mice at D14. Data representative of three independent experiments.

C. ELISA quantification of anti-NP antibodies detected by binding to $NP_{1\text{-}9}$ and $NP_{>20}$ antigens respectively (n=4). Data representative of two independent experiments.

D. Quantification of CD45.2$^+$ GC B cells from spleens and Peyer's patches of Aicda-WT (n=4) and Aicda-Tfam (n=5) 50:50 competitive bone marrow chimeras following SRBC immunisation at Day 7, normalised to CD45.1 WT GC B cell proportions.

E. Representative flow cytometry plots of tdTomato and TFAM fluorescence in TAT-Cre treated and in vitro-stimulated B cells from Rosa-WT (n=2) and Rosa-Tfam mice (n=2). Data representative of two independent experiments.

F. Quantification of viable cell percentages (LiveDead eFluor780$^-$) in tdTomato$^+$ CD19$^+$ pre-gated Rosa-WT and Rosa-Tfam B cells. Data representative of two independent experiments.

G. Representative flow cytometry histogram of CTV fluorescence in TAT-Cre treated and in vitro-stimulated tdTomato$^+$ CD19$^+$ B cells from Rosa-WT and Rosa-Tfam mice. Data representative of two independent experiments.

Statistical significance was calculated by unpaired two-tailed t-test (A-D).

Supplementary figure 5

S5A

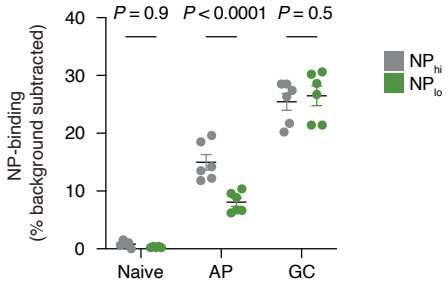

S5B

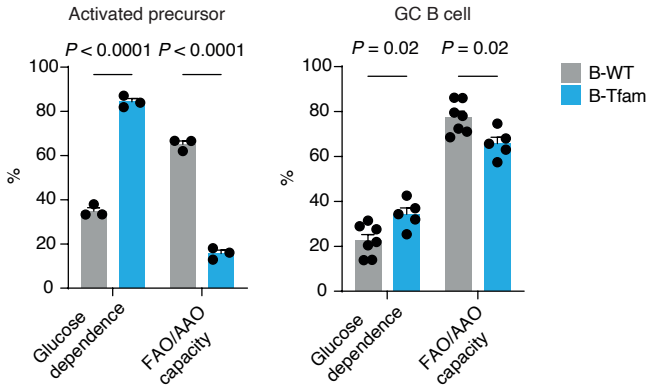

S5

A. Quantification of NP-binding rates of naïve B cells, APs, and GC B cells isolated from Aicda-WT to high (NP_{hi}) and low NP (NP_{lo})-APC conjugates corresponding to low and high affinity to NP respectively. Non-specific background was subtracted based on labelling in unimmunised mice. Data pooled from two independent experiments.

B. Quantification of glucose dependence and FAO/AAO capacity of cells from (figure 3F).

Statistical significance was calculated by two-way ANOVA with Šidák's multiple comparison test (A-B).

Supplementary figure 6

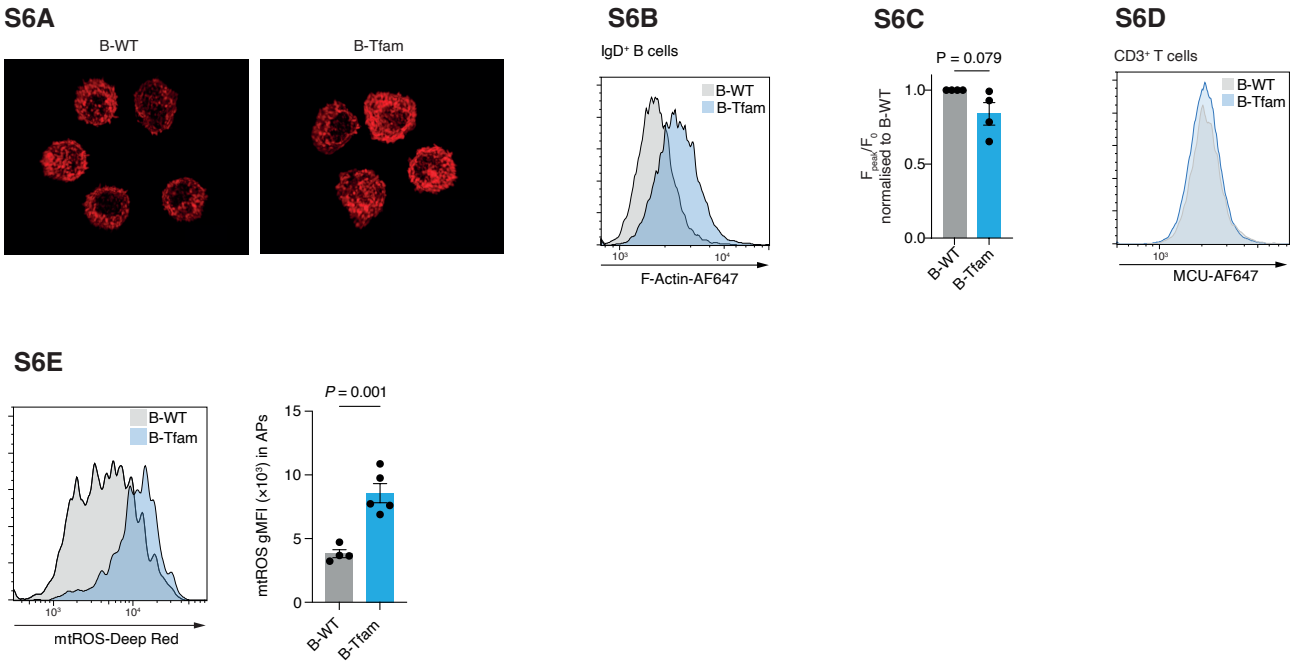

S6

A. 3D Airyscan confocal image of F-actin phalloidin-stained total B cells from unimmunised B-WT and B-Tfam mice.

B. Representative flow cytometry histogram of F-actin phalloidin fluorescence of IgD+ B cells from unimmunised B-WT and B-Tfam mice. Representative of two independent experiments.

C. Quantification of fold change in geometric MFI at peak normalised to baseline (F_0, 0-30s pre-stimulation). Experiment was run as technical duplicates in four independent replicate experiments consisting of one B-Tfam and one wild-type mouse. Data points from B-Tfam were normalised to wild-type data run in the same batch.

D. Representative flow cytometry histogram of MCU fluorescence of CD3+ T cells from unimmunised B-WT and B-Tfam mice. Representative of three independent experiments.

E. Representative flow cytometry histogram of mtROS Deep Red fluorescence in IgD+ GL-7+ cells from immunised B-WT (n=4) and B-Tfam mice (n=5). Data representative of two independent experiments.

Statistical significance was calculated by unpaired two-tailed t-test (C, E).

Supplementary figure 7

S7A

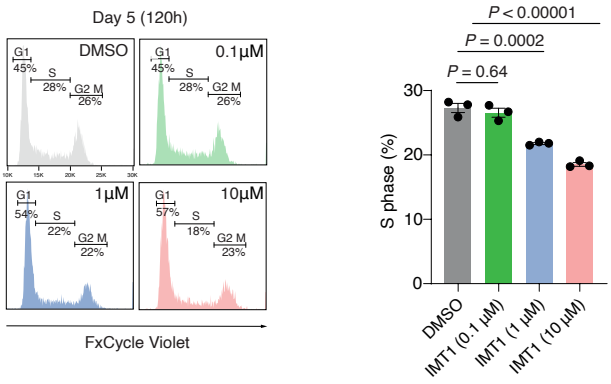

S7

A. Flow cytometry-based cell cycle stage characterisation (G1, S, G2-M) in Daudi cells at 120h following IMT1 treatment. Quantification of Daudi cells in S phase, representative of two independent experiments.

Statistical significance was calculated by ordinary one-way ANOVA with Tukey's multiple comparisons test.